The following publication J. Fang, B. Xu, X. Liu and L. -T. Hsu, "Multipath Parameter Estimation Using GNSS Receiver Doppler Measurements," in IEEE Transactions on Aerospace and Electronic Systems, vol. 62, pp. 9395-9412, 2026 is available at https://doi.org/10.1109/TAES.2026.3683035.

Multipath parameter estimation using GNSS receiver Doppler measurements

Jingxiaotao Fang
Bing Xu, Member, IEEE
Xikun Liu
Li-Ta Hsu, Senior Member, IEEE
The Hong Kong Polytechnic University, HK

***Abstract*— The accuracy and robustness of global navigation satellite systems (GNSS) degrade in urban environments, which particularly affects low-cost GNSS users. Among various multipath mitigation techniques, signal parameter estimation enables the identification and characterization of interference, facilitating its removal from the navigation solution. This study models multipath interference in the receiver's frequency-locked loop (FLL) to characterize Doppler measurement errors induced by multipath. Subsequently, a Doppler-based multipath parameter estimation method is proposed using a nonlinear least squares (NLS) algorithm to estimate the Doppler frequency, carrier phase, and signal strength of both line-of-sight (LOS) and reflected signals. Experiments were conducted in urban areas of Hong Kong, with ray-tracing techniques utilizing ground-truth data as a benchmark for assessing multipath detection and parameter estimation accuracy. The proposed method is also compared with established signal quality monitoring (SQM) metrics and the multipath estimating delay-locked loop (MEDLL) technique. Results demonstrate that the Doppler-based approach enhances multipath detection efficiency, reduces false alarm rates, and provides more reliable parameter estimation, particularly in dynamic user scenarios.**

***Index Terms*—GNSS multipath, urban, detection, parameter estimation, mitigation, receiver, FLL**

I. INTRODUCTION

Global navigation satellite systems (GNSS) play a vital role in positioning, navigation, and timing applications. However, the growing dependence on GNSS in modern urban environments raises concerns about its vulnerabilities. One significant challenge is the multipath phenomenon, in which signals propagate along multiple paths due to reflections from surrounding obstacles. The superposition of line-of-sight (LOS) and reflected signals introduces biases in signal synchronization parameters, such as code phase and Doppler frequency, leading to positioning errors. For low-cost standalone receivers, relying on external hardware for multipath mitigation may be impractical. Consequently, researchers have developed various techniques at different stages of receiver processing to effectively mitigate multipath interference.

Many multipath mitigation techniques have been developed at the receiver tracking level, where the receiver continuously estimates the time evolution of signal synchronization parameters. The relationship between pseudorange measurement errors and the code phase difference between LOS and reflected signals has been extensively studied, with the widely used multipath error envelope (MEE) providing a foundational framework [1, 2, 3]. Consequently, multipath effects can be mitigated by modifying the correlator structure, as seen in techniques such as narrow correlators [4, 5], high resolution correlators [6], extended double-delta correlators [7], and vision correlators [8]. Some techniques perform extensive searches in the code phase domain, identifying multiple distinguishable correlation peaks corresponding to different signal components under multipath interference. For instance, [9] introduced a deep network correlator to filter out multipath effects on the autocorrelation function. In addition, machine learning classifiers have been applied directly to multi-correlator outputs [10]. Other methods estimate the parameters of incoming signals by modeling multipath effects on correlator values and applying maximum likelihood (ML) techniques. The multipath estimating delay-locked loop (MEDLL) exemplifies this approach by utilizing a bank of correlators to determine the delays and amplitudes of individual multipath signals [11]. An extension of this idea is the coupled amplitude delay lock loop (CADLL), which jointly tracks both the amplitude and delay of multipath components, thereby improving robustness in noisy and dynamic environments [12]. A low-complexity multipath parameter estimation method for multicorrelator receivers was proposed in [13], based on log-likelihood maximization using a grid search approach. Additionally, [14] introduced a random forest-based estimator to enhance multipath parameter estimation accuracy. However, the accuracy of parameter estimation in these methods remains constrained by the number and spacing of correlators, leading to significant computational complexity in real-time applications [15].

Mitigating multipath using existing or commonly available receiver outputs presents an alternative that avoids modifications to receiver design. Signal quality monitoring (SQM) techniques, such as delta and ratio metrics, are widely employed to detect abnormalities in receiver outputs caused by multipath interference [16, 17].

Manuscript received XXXXX 00, 0000; revised XXXXX 00, 0000; accepted XXXXX 00, 0000.
This work was supported in part by the National Natural Science Foundation of China (NSFC) under Grant 62103346, and in part by PolyU Startup Fund for New Recruits (Project No.: P0049535).

Jingxiaotao Fang is with The Hong Kong Polytechnic University, HK (e-mail: jingxiaotao2.fang@connect.polyu.hk); Bing Xu is with The Hong Kong Polytechnic University, HK (e-mail: pbing.xu@polyu.edu.hk); Xikun Liu is with The Hong Kong Polytechnic University, HK (e-mail: xi-kun.liu@connect.polyu.hk); Li-Ta Hsu is with The Hong Kong Polytechnic University, HK (e-mail: lt.hsu@polyu.edu.hk). *(Corresponding author: Bing Xu).*

0018-9251 © 2024 IEEE

[18] employs a graph-based deep learning model that jointly predicts satellite and measurement weights in urban. Receiver autonomous integrity monitoring (RAIM) is another widely used approach that identifies outliers based on the statistical characteristics of receiver measurements [19]. Once detected, satellites contributing to these anomalies can be excluded from the position, velocity, and time (PVT) solution to improve accuracy. Another approach involves applying weighting schemes to mitigate multipath errors in receiver navigation, such as satellite elevation-dependent and carrier-to-noise density ratio (C/N_0)-dependent models [20, 21]. However, mitigation methods relying on de-weighting or exclusion may degrade navigation geometry, potentially reducing overall positioning accuracy. Furthermore, even high-elevation or strong-C/N_0 signals can experience severe multipath effects in complex environments, limiting the effectiveness of these approaches [22].

Existing research reveals several noticeable gaps in multipath mitigation. While extensive work has been done to understand the impact of multipath on pseudorange measurements, leading to the development of the widely used MEE, the effects of multipath on Doppler frequency and pseudorange rate measurements have been overlooked. In particular, the literature exhibits conflicting views on the multipath-induced Doppler measurement error. On one hand, numerous studies have reported non-negligible Doppler frequency differences between the LOS and reflected signals under various conditions, including static receiver [23], varying user velocity [24, 25], and different signal ray geometries [26]. On the other hand, many existing models assume the Doppler frequency difference to be negligible [15, 27, 28]. To address this discrepancy, the author's previous work theoretically analyzed receiver frequency tracking performance under multipath interference [29], demonstrating that Doppler measurements can become erroneous due to the interaction of multiple signals during frequency tracking.

In the field of advanced GNSS positioning algorithms, the need for corrected Doppler measurements has been highlighted in many studies. For example, errors in Doppler-based velocity estimation can lead to incorrect integrated results in factor graph optimization (FGO) [30, 31]. Additionally, Doppler-aided positioning algorithms are widely implemented in GNSS receivers, where pseudoranges and Doppler measurements are jointly processed using weighted least squares or Kalman filter (KF) algorithms [32]. Other techniques leverage Doppler measurements to smooth code-based positioning, enhancing both accuracy and robustness [33, 34]. Furthermore, Doppler-smoothed code measurements play a crucial role in resolving integer ambiguity during instantaneous real-time kinematic (RTK) positioning [35]. Therefore, there is a critical need for a multipath detection and mitigation method in Doppler measurement.

This study proposes a novel multipath parameter estimation method that leverages receiver Doppler measurements. In previous work, we established a theoretical foundation by modeling Doppler measurement error and validating the error using a commercial receiver [29]. Building on this theoretical analysis, this work extends the model to directly link Doppler measurement errors with multiple incoming signal parameters. A distinctive Doppler oscillation feature in the time domain is identified, characterized by differences in the parameters of incoming signal components. By exploiting this Doppler oscillation feature, our proposed method enables accurate signal parameter estimation, allowing for the detection of reflected signals and the correction of Doppler measurements for better receiver navigation. The key contributions are summarized in Fig. 1. A nonlinear least

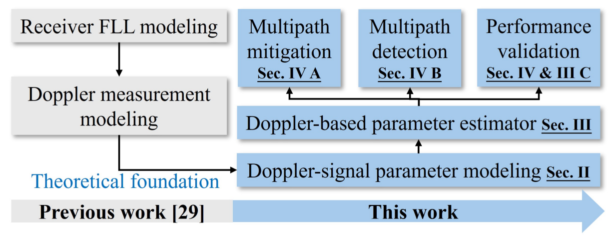

Fig. 1. Summary of key contributions.

squares (NLS) estimator is introduced to estimate Doppler frequencies, carrier phase, and signal strength of incoming signal rays. The proposed method is validated through pedestrian and vehicle experiments conducted in urban environments. The accuracy of signal parameter estimation is assessed by comparing the estimated parameters with those obtained from ray-tracing simulations. The ray-tracing technique, which integrates 3-dimensional (3D) building models and user ground truth data, calculates the most probable signal propagation paths from the satellite to the receiver and serves as a benchmark for performance evaluation [36]. Furthermore, the proposed method is evaluated against traditional correlator-based multipath detection and parameter estimation techniques, including SQM metrics and MEDLL. In addition, performance assessments are conducted under varying levels of noise interference and different sampling sizes through simulations, with results benchmarked against the Cramér–Rao lower bound (CRLB). Since Doppler measurement is the standard receiver output and does not require modifications to the receiver architecture, the proposed method is cost-effective for low-cost commercial GNSS receivers.

The contributions of this work are summarized as follows:

1) Building on prior work of multipath-induced Doppler error characterization, this work derives a signal-parameter-based Doppler error model and applies it for error mitigation.
2) Propose a novel multipath signal parameter estimator and detector using receiver Doppler measurements.
3) The parameter estimator and multipath detector are validated through real-world experiments, with accuracy assessed using ray-tracing and compared to SQM and MEDLL. The collected raw data is open-sourced.

4) Derive the CRLB to evaluate estimator performance under varying noise levels and sample sizes.

II. MULTIPATH EFFECT IN FLL

A. Modeling

Our previous research theoretically examined the receiver frequency-locked loop (FLL) under multipath interference [29]. Building on this foundation, the present study develops a theoretical model that explicitly links Doppler measurements to multipath signal parameters, thereby enabling parameter estimation of incoming signals. We consider a common multipath scenario in which a single channel receives both a LOS signal and a single reflected signal. The resulting compound signal $S(t)$ received in the antenna can be modeled as:

$$\begin{aligned} &S(t) = \\ &\sqrt{2C_{LOS}}D(t-\tau_{LOS})x(t-\tau_{LOS})\sin(\omega_{LOS}t+\vartheta_{LOS}) \\ &+\sqrt{2C_{ref}}D(t-\tau_{ref})x(t-\tau_{ref})\sin(\omega_{ref}t+\vartheta_{ref})+v(t) \end{aligned} \tag{1}$$

where t represents the continuous sample time. $D(\cdot)$ and $x(\cdot)$ are the navigation data and pseudo-random noise (PRN) code, respectively. The amplitudes of the LOS and reflected signals are given by $\sqrt{2C_{LOS}}$ and $\sqrt{2C_{ref}}$, respectively. τ_{LOS}, ω_{LOS}, ϑ_{LOS} correspond to the code delay, angular frequency, and initial carrier phase of the LOS signal, while τ_{ref}, ω_{ref}, ϑ_{ref} represent those of the reflected signal. $v(\cdot)$ is the additive Gaussian white noise.

Typical receiver operations include acquisition, tracking, and navigation. This study primarily focuses on the receiver frequency tracking loop. Initially, the incoming signal is correlated with the receiver's local replica. Then, the integrate-and-dump process removes high-frequency components and integrates correlation values over a predefined coherent integration time [1]. Finally, the ideal in-phase (I) and quadrature-phase (Q) channel prompt correlator outputs under multipath interference are given as [29]:

$$\begin{aligned} I_P(n) &= A_{LOS}(n)\cos\Delta\phi_{LOS}(n) \\ &\quad + A_{ref}(n)\cos\Delta\phi_{ref}(n) + v_{P,i}(n) \end{aligned} \tag{2}$$

$$\begin{aligned} Q_P(n) &= A_{LOS}(n)\sin\Delta\phi_{LOS}(n) \\ &\quad + A_{ref}(n)\sin\Delta\phi_{ref}(n) + v_{P,q}(n) \end{aligned} \tag{3}$$

where n represents the n-th epoch, and the duration between two epochs is determined by the coherent integration time T. $A_{LOS}(n)$ and $A_{ref}(n)$ are the amplitudes of the LOS and reflected signal components at n, respectively. $\Delta\phi_{LOS}(n)$ and $\Delta\phi_{ref}(n)$ are the carrier phase errors of the LOS signal and reflected signal, respectively. $v_{P,i}(n)$ and $v_{P,q}(n)$ are the prompt correlator noises, and are modelled as independent terms following a centred Gaussian distribution. The amplitudes can be expressed as a function of the frequency error as [29, 37]:

$$A_{LOS}(n) \approx N\sqrt{C_{LOS}}R(\Delta\tau_{LOS})\mathrm{sinc}\left(\left(f_{LOS}-f_0^-\right)T\right) \tag{4}$$

$$A_{ref}(n) \approx N\sqrt{C_{ref}}R(\Delta\tau_{ref})\mathrm{sinc}\left(\left(f_{ref}-f_0^-\right)T\right) \tag{5}$$

where N represents the number of samples within the coherent integration time, and $R(\cdot)$ denotes the autocorrelation function (ACF). $\Delta\tau_{LOS}$ and $\Delta\tau_{ref}$ are the code phase errors of the LOS and reflected signals, respectively. f_{LOS}, f_{ref}, and f_0^- represent the instantaneous Doppler frequency of the LOS signal, reflected signal, and predicted receiver local signal, respectively. The superscript $(-)$ represents the receiver's predicted value. In the closed-loop tracking loop, the phase error $\Delta\phi_{LOS}(n)$ and $\Delta\phi_{ref}(n)$ can be expressed as the time integral of the Doppler error [38]:

$$\Delta\phi_{LOS}(n) \approx \int_{t_0}^{t_n} 2\pi\left(f_{LOS}(t)-f_0^-(t)\right)dt + \Delta\phi_{LOS}(t_0) \tag{6}$$

$$\Delta\phi_{ref}(n) \approx \int_{t_0}^{t_n} 2\pi\left(f_{ref}(t)-f_0^-(t)\right)dt + \Delta\phi_{ref}(t_0) \tag{7}$$

where $t_n = t_0 + nT$. $\Delta\phi_{LOS}(t_0)$ and $\Delta\phi_{ref}(t_0)$ are the initial phase errors of the LOS signal and reflected signal at the starting time t_0, respectively. The phase discriminator output quantifies the carrier phase difference between the incoming signal and the local carrier, and is filtered with a loop filter to decrease the impact of noise. For clarity, we first consider an ideal, noise-free discriminator output. The impact of noise is addressed in subsequent sections. Based on (2) and (3), the phase discriminator output can be expressed as:

$$\begin{aligned} \Delta\phi_{com}(n) &= \arctan\left(\frac{Q_P(n)}{I_P(n)}\right) \\ &= \arctan\left(\frac{\alpha(n)\sin\Delta\phi_{LOS}(n)+\sin\Delta\phi_{ref}(n)}{\alpha(n)\cos\Delta\phi_{LOS}(n)+\cos\Delta\phi_{ref}(n)}\right) \end{aligned} \tag{8}$$

where $\Delta\phi_{com}(n)$ is the carrier phase error of the compound signal. $\alpha(n)$ denotes the amplitude ratio between the LOS signal vector and the reflected signal vector, and is defined as $\alpha(n) = A_{LOS}(n)/A_{ref}(n)$.

The following sections first examine a common scenario in which the reflected signal has a lower amplitude than the direct signal. This attenuation typically results from power loss and signal delay caused by reflection [39]. Special cases in which the reflected signal is stronger than the direct signal will be discussed in Section III. B. Using the trigonometric identity, equation (8) can be expressed as the sum of two arctangent terms:

$$\arctan\left(\frac{A+B}{1-AB}\right) = \arctan(A) + \arctan(B) \tag{9}$$

where A and B are limited by the principal range of the arctangent functions and follow $1-AB \neq 0$. Applying this identity to (8) and considering scenarios where $\alpha(n)$ exceeds 1, it can be rewritten as:

$$\Delta\phi_{com}(n) = \underbrace{\arctan\left(\frac{\sin\Delta\phi_{LOS}(n)}{\cos\Delta\phi_{LOS}(n)}\right)}_{\Delta\phi_{LOS}(n)} + \underbrace{\arctan\left(\frac{\sin\left(\Delta\phi_{ref}(n) - \Delta\phi_{LOS}(n)\right)}{\alpha(n) + \cos\left(\Delta\phi_{ref}(n) - \Delta\phi_{LOS}(n)\right)}\right)}_{\Delta\phi_{MP}(n)} \tag{10}$$

This equation demonstrates that the carrier phase error of the compound signal consists of the carrier phase error of the LOS signal, $\Delta\phi_{LOS}(n)$, and a function represented by $\Delta\phi_{MP}(n)$. The expression for $\Delta\phi_{MP}(n)$ is mathematically equivalent to the well-known carrier phase multipath error described in [40]. In FLL, the two-arctangent and four-arctangent discriminators are commonly used to monitor the rate of change of the phase error [37, 40]. Based on equations (6) and (10), the frequency discriminator output is obtained as:

$$\begin{aligned}\delta f_{com}(n) &\approx \frac{\Delta\phi_{com}(n) - \Delta\phi_{com}(n-1)}{2\pi T} \\ &\approx f_{LOS}(n) - f_0^-(n) + \frac{\Delta\phi_{MP}(n) - \Delta\phi_{MP}(n-1)}{2\pi T}\end{aligned} \tag{11}$$

$f_{\cdot}(n)$ denotes the epoch-averaged values over the n-th epoch. The discriminator's output serves as the input to the loop filter. Different loop filters, characterized by their design and parameter settings, influence loop stability and tracking performance [1]. To simplify the theoretical analysis, we assume that no additional state variables (e.g., Doppler acceleration) are introduced between adjacent epochs, and that the discriminator output can be approximated as directly corresponding to the frequency corrections applied by the numerically controlled oscillator (NCO). In Section IV, a second-order PLL filter is employed in the GNSS receiver implementation. Consequently, the receiver-predicted Doppler frequency is adjusted by the NCO output, and the receiver's Doppler measurement at n can be expressed as:

$$f_0(n) = f_0^-(n) + \delta f_{com}(n) \tag{12}$$

Substitute (11) into (12), the receiver Doppler measurement under multipath interference can be summarized:

$$f_0(n) = f_{LOS}(n) + \frac{\Delta\phi_{MP}(n) - \Delta\phi_{MP}(n-1)}{2\pi T} \tag{13}$$

Equation (14) is the full expression of equation (13), which describes the relationship between the receiver Doppler measurement and the parameters of the LOS and reflected signals. $v_{mea}(n)$ is the Doppler measurement noise. The deviations and transformations involved are explained in detail in Appendix A. $f_{shift}(\cdot) = f_{ref}(\cdot) - f_{LOS}(\cdot)$ and $\Delta\phi_{shift}(\cdot) = \Delta\phi_{ref}(\cdot) - \Delta\phi_{LOS}(\cdot)$ are defined as the *frequency shift* and *initial carrier phase shift* of the reflected signal, respectively. It was observed that the Doppler multipath error is influenced by the frequency shift of the reflected signal, the initial carrier phase shift of the reflected signal, and the amplitude ratio. Analyzing the performance of the Doppler multipath error is crucial for understanding the overall performance of receiver Doppler measurements under multipath interference.

B. Analysis of Doppler multipath error

This section aims to visualize the dynamic behavior of the Doppler multipath error through simulation tests based on the theoretical model (14). Fig. 2 presents a noise-free simulation of the receiver Doppler measurement in both the time domain and histogram form. Incoming signal 1 represents the LOS signal, characterized by a constant Doppler frequency of 10 Hz. Incoming signals 2 and 3, representing the reflected signals, have Doppler frequencies set to 15 Hz and 20 Hz, respectively. The power of each reflected signal is 3 dB lower than that of the LOS signal. Fig. 2 (a) illustrates that when the signal parameters of the incoming signals remain constant, the receiver Doppler measurement exhibits periodic oscillations around the LOS signal, with fixed maximum and minimum points. The frequency and amplitude of these oscillations increase as the frequency shift of the reflected signal becomes larger. Additionally, the Doppler oscillation frequency is equal to the frequency shift of the reflected signal, as derived from equation (14), a conclusion that is consistent with the findings in [41]. Fig. 2 (b) shows that the receiver Doppler measurement follows a skewed distribution, with most samples concentrated around the Doppler frequency of the LOS signal. The peak of occurrence does not coincide with the Doppler frequencies of any individual signal component. Consequently, the frequency information of the incoming signals becomes distorted during receiver tracking, making it challenging to directly estimate the signal component frequencies using the Fast Fourier Transform (FFT) method. As a result, FFT-based methods typically require raw signal or correlator-level data to accurately extract signal components [42, 43, 44].

For cases where $\alpha(n) > 1$, the maximum and minimum Doppler measurements under multipath interference are theoretically derived as:

$$f_0(n) = \begin{cases} f_{LOS}(n) + \left|\frac{f_{shift}(n)}{1-\alpha(n)}\right|, \text{maximun} \\ f_{LOS}(n) + \left|\frac{f_{shift}(n)}{1+\alpha(n)}\right|, \text{minimum} \end{cases} \tag{15}$$

The detailed derivations are provided in Appendix B. Thus, it can be concluded that the extreme points of the Doppler oscillation are determined by the frequency shift and amplitude ratio. A larger frequency shift results in a higher oscillation amplitude, which aligns with the simulation results shown in Fig. 2. Conversely, a larger amplitude ratio leads to a smaller oscillation amplitude, consistent with the expectation that a weaker reflected signal induces a smaller Doppler multipath error.

$$f_0(n) = f_{LOS}(n) + \underbrace{f_{shift}(n) \cdot \left(\frac{\alpha(n)\cos\left(\int_{t_0}^{t_n} 2\pi f_{shift}(t)dt + \Delta\phi_{shift}(t_0)\right) + 1}{\alpha^2(n) + 2\alpha(n)\cos\left(\int_{t_0}^{t_n} 2\pi f_{shift}(t)dt + \Delta\phi_{shift}(t_0)\right) + 1} \right)}_{\text{Doppler Multipath Error: } f_{MP}(n)} + v_{mea}(n) \quad (14)$$

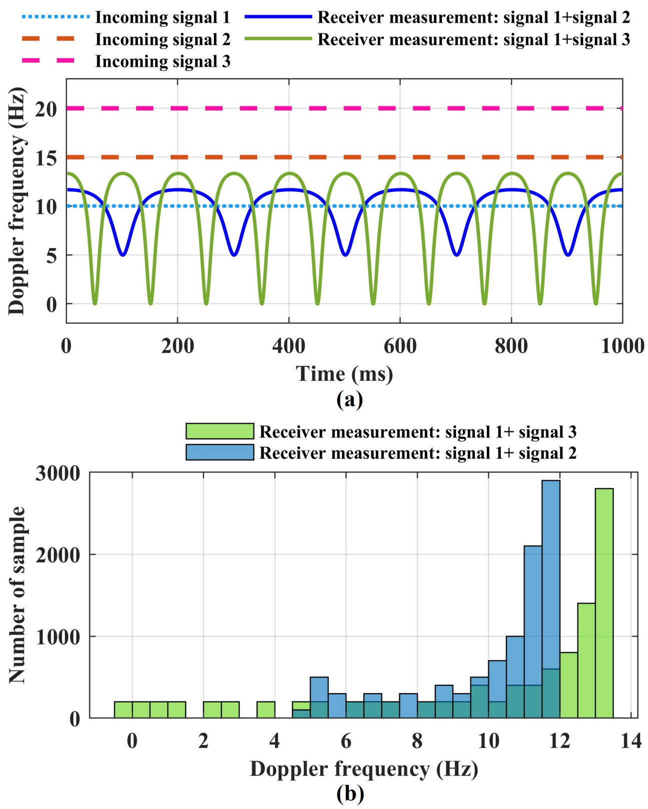

Fig. 2. (a) Time-domain simulation of the receiver's Doppler measurement under multipath reception, with the powers of incoming signals 2 and 3 each set 3 dB lower than that of incoming signal 1. (b) Histogram of the simulated receiver Doppler measurements under multipath reception.

C. Error Envelopes

The well-known MEE or pseudorange (PR) error envelopes describe the worst-case impact of multipath effects on code tracking in a defined scenario [1]. These envelopes illustrate the relationship between PR error and the reflected signal path delay (code phase shift). The authors' previous work introduced pseudorange rate (PR rate) and Doppler error envelopes [29]. This section extends that analysis to compare the sensitivity of PR and PR rate errors to multipath interference, which is valuable for developing multipath detection and mitigation strategies across various scenarios.

Since the receiver Doppler measurement exhibits dynamic oscillations, the error envelopes are plotted at the first epoch in which the reflected signal is injected. Fig. 3 compares the PR error and PR rate error for a binary phase shift keying (BPSK) signal in the code phase domains. The Y-axis represents the code phase shift of the reflected signal relative to the direct signal (τ_{shift}), while the X-axis represents the frequency shift of the reflected signal relative to the direct one, normalized by the coherent integration time. A normalized frequency shift value of 1 corresponds to the pull-in range of the FLL discriminator, which is given by $1/T$. During the simulations, an early-

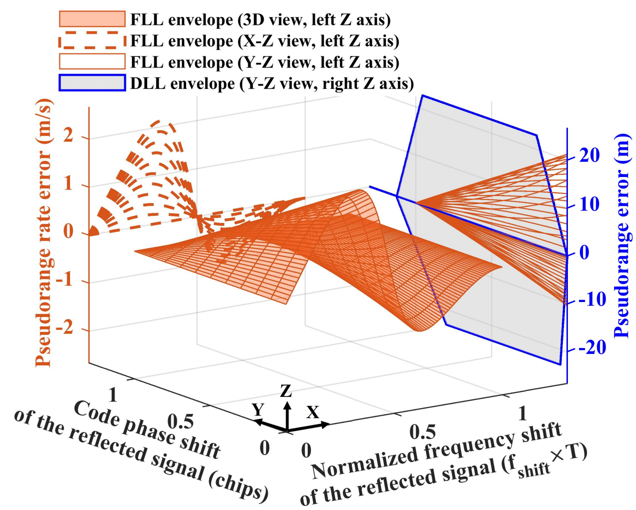

Fig. 3. Comparison between the PR error and PR rate error envelopes.

minus-late discriminator is employed with an early-to-late correlator spacing of 0.25 chips. In the Y-Z view plots of Fig. 3, the shaded area in the PR error envelope represents all possible values of the carrier phase error, while each line in the PR rate error envelope corresponds to potential values of the frequency shift of the reflected signal. The figure reveals that the maximum PR rate error occurs when τ_{shift} is zero, at which point the PR error is minimized. As τ_{shift} increases, the PR error initially increases, then stabilizes, and eventually decreases, whereas the PR rate error continuously decreases. Notably, the minimum PR rate error and the maximum PR error occur at different τ_{shift} values.

Therefore, the sensitivity of PR/correlator-based and Doppler-based detection and mitigation methods can be assessed. Short-delay reflected signals can produce significant Doppler measurement errors and oscillations, especially when they are accompanied by strong signal power and non-negligible Doppler frequency shifts. This is because the reflected signal with shorter delay experiences less attenuation by the autocorrelation function, resulting in stronger contributions to the signal vector tracked by the FLL. Conversely, when the reflected signal has a large delay, leading to substantial amplitude attenuation, its impact on Doppler measurements diminishes. In such cases, PR/correlator-based multipath detection and mitigation methods may be the preferred choice.

III. DOPPLER-BASED MULTIPATH MITIGATION METHOD

This work proposes a novel multipath detection and mitigation method that leverages signal parameter estimation utilizing the unique Doppler oscillation features. The flowchart of this work is summarized in Fig. 4. Section II starts at the base-band level, deriving a Doppler measurement model that captures the characteristic oscillation produced by a single dominant reflection. This model feeds directly into the proposed Doppler-based nonliear least squares (D-NLS) estimator, introduced in Sections III A and B. Section III C quantifies the achievable accuracy by deriving the CRLB and verifying it with Monte-Carlo simulations over a range of C/N_0 levels and sample sizes. Section IV A then applies the method to pedestrian and vehicular data, validating the estimated parameters against ray-tracing ground truth, while Section IV B benchmarks the proposed approach against state-of-the-art multipath detectors and estimators, demonstrating its superior performance in dynamic urban scenarios.

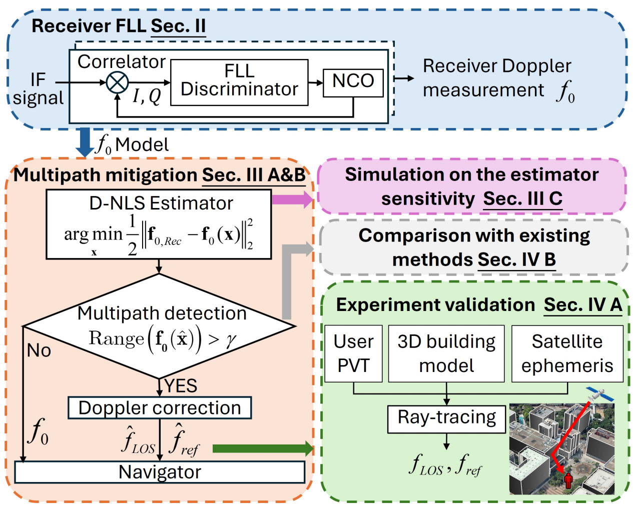

Fig. 4. Flowchart of the proposed method and organization of this work.

A. Doppler-based nonlinear least squares estimator

Let the unknown parameters, LOS Doppler frequency, Doppler shift, initial carrier phase shift, and amplitude ratio, be denoted as:

$$\mathbf{x} = \left[\tilde{f}_{LOS}, \tilde{f}_{shift}, \Delta\tilde{\phi}_{shift}, \tilde{\alpha}\right]^{\mathsf{T}} \in \mathbb{R}^4 \tag{16}$$

where the tilde symbol ($\sim$) represents estimation candidates. These parameters are assumed to remain relatively stable within a given estimation window and can be estimated using a sufficient number of *receiver Doppler measurements*. The receiver Doppler measurement refers to the Doppler frequency output from a real receiver, denoted as $\mathbf{f}_{0,Rec}$ and modeled in (14). For an estimation window spanning epochs 1 to M, the receiver Doppler measurements $\mathbf{f}_{0,Rec}$ and the estimated Doppler measurement $\mathbf{f}_0(\mathbf{x})$ are given by:

$$\mathbf{f}_{0,Rec} = \left[f_{0,Rec}(1), f_{0,Rec}(2), \ldots, f_{0,Rec}(M)\right]^{\mathsf{T}} \tag{17}$$

$$\mathbf{f}_0(\mathbf{x}) = \left[\tilde{f}_0(1;\mathbf{x}), \tilde{f}_0(2;\mathbf{x}), \ldots, \tilde{f}_0(M;\mathbf{x})\right]^{\mathsf{T}} \tag{18}$$

In the algorithmic implementation, the noise-free estimated Doppler measurement at epoch n, consistent with the model in (14), is expressed as:

$$\tilde{f}_0(n;\mathbf{x}) = \tilde{f}_{LOS} + \tilde{f}_{shift}\left(\frac{\tilde{\alpha}\cos\left(\sum_1^n 2\pi T\tilde{f}_{shift} + \Delta\tilde{\phi}_{shift}\right) + 1}{\tilde{\alpha}^2 + 2\tilde{\alpha}\cos\left(\sum_1^n 2\pi T\tilde{f}_{shift} + \Delta\tilde{\phi}_{shift}\right) + 1}\right) \tag{19}$$

1) Cost Function: The proposed estimator aims to estimate the unknown parameters in (16) by minimizing the residual between the received and the estimated Doppler measurements. The residual is defined as:

$$\mathbf{r}(\mathbf{x}) = \mathbf{f}_{0,Rec} - \mathbf{f}_0(\mathbf{x}) \in \mathbb{R}^M \tag{20}$$

The proposed D-NLS estimator is formulated as:

$$\hat{\mathbf{x}} = \underset{\mathbf{lb}\le\mathbf{x}\le\mathbf{ub}}{\arg\min} \frac{1}{2}\|\mathbf{r}(\mathbf{x})\|_2^2 \tag{21}$$

The hat symbol ($\wedge$) indicates the optimal estimate. $\|\cdot\|_2$ indicates the Euclidean norm. $\mathbf{lb}, \mathbf{ub} \in \mathbb{R}^4$ are the bound vectors on each unknown parameter. $\Delta\tilde{\phi}_{shift}$ and $\tilde{\alpha}$ are limited to $[-\pi, \pi]$ and [1, 30], respectively. Boundaries of $\tilde{f}_{LOS}$ and $\tilde{f}_{shift}$ are set to the size of 20 Hz around the initialization values, which are derived in the following part. Then, the Doppler frequency of the reflected signal during this estimation window can be calculated as:

$$\hat{f}_{ref} = \hat{f}_{LOS} + \hat{f}_{shift} \tag{22}$$

The D-NLS estimator provides several key results directly: the Doppler frequencies of the LOS and reflected signals, the initial carrier phase shift, the amplitude ratio, and the curve-fitting residuals.

2) Optimization Method: The estimator employs MATLAB's `lsqnonlin` solver, which implements a trust-region-reflective algorithm combining dogleg and truncated-conjugate-gradient updates under simple bound constraints [45]. Mathematically, the trust-region subproblem for iteration k is typically stated:

$$\mathbf{s}^{(k)} = \underset{\|\mathbf{D}\mathbf{s}\|_2\le\Delta_k}{\arg\min} \frac{1}{2}\left\|\mathbf{J}^{(k)}\mathbf{s} + \mathbf{r}^{(k)}\right\|_2^2 \tag{23}$$

where Δ_k is the trust-region radius and is updated according to MATLAB's default thresholds. $\mathbf{D} = diag(\mathbf{d})$ is the scaling matrix with $d_i = \frac{1}{u_i - \ell_i}$, $u \in \mathbf{ub}, \ell \in \mathbf{lb}$, to normalize each parameter to [0,1]. $\mathbf{r}^{(k)} = \mathbf{r}(\mathbf{x}^{(k)})$ is the residual vector at k defined by (20). Bounds on $\mathbf{x}$ are enforced by reflecting any component $\mathbf{x}^{(k)} + \mathbf{s}^{(k)}$ that would violate the bounds. $\mathbf{J}^{(k)} = \mathbf{J}(\mathbf{x}^{(k)})$ is the Jacobian matrix. Due to the complicated nonlinear expressions of Doppler measurement, no analytic derivatives are provided to the algorithm. MATLAB approximates the Jacobian matrix by forward finite differences:

$$\mathbf{J}^{(k)} = \frac{\partial \mathbf{r}(\mathbf{x}^{(k)})}{\partial \mathbf{x}} \in \mathbb{R}^{M\times 4} \tag{24}$$

For example, for parameter x_i at epoch n:

$$[\mathbf{J}^{(k)}]_{n,i} = \frac{\partial r_n(\mathbf{x}^{(k)})}{\partial x_i} = -\frac{\partial \tilde{f}_0\left(n; \mathbf{x}^{(k)}\right)}{\partial x_i} \tag{25}$$

where

$$\frac{\partial \tilde{f}_0\left(n; \mathbf{x}^{(k)}\right)}{\partial x_i} \approx \frac{\tilde{f}_0\left(n; x_i^{(k)} + \varepsilon \mathbf{e}_i\right) - \tilde{f}_0\left(n; x_i^{(k)}\right)}{\varepsilon} \tag{26}$$

ε is the default small perturbation such as 10^{-6} and $\mathbf{e}_i$ is the ith standard basis vector in $\mathbb{R}^4$.

At each iteration, the residual $\mathbf{r}^{(k)}$ is computed and $\mathbf{J}^{(k)}$ is approximated using forward finite differences. The trust-region step $\mathbf{s}^{(k)}$ is obtained by solving the subproblem defined in (23). The reduction ratio

$$\rho^{(k)} = \frac{\left\|\mathbf{r}(\mathbf{x}^{(k)})\right\|_2^2 - \left\|\mathbf{r}(\mathbf{x}^{(k)} + \mathbf{s}^{(k)})\right\|_2^2}{\left\|\mathbf{r}(\mathbf{x}^{(k)})\right\|_2^2 - \left\|\mathbf{J}(\mathbf{x}^{(k)})\mathbf{s}^{(k)} + \mathbf{r}(\mathbf{x}^{(k)})\right\|_2^2} \tag{27}$$

measures how well the linearized model predicts the actual residual reduction. If $\rho^{(k)} \geq 0.75$, the iteration step is accepted and the trust-region radius Δ is increased. If $0.75 \geq \rho^{(k)} \geq 0.25$, the step is accepted but Δ is unchanged. Otherwise, this step is rejected and Δ is reduced. Iteration stops when either the step size $\left\|\mathbf{s}^{(k)}\right\|_2$ or the cost function $\left\|\mathbf{r}^{(k)}\right\|_2$ falls below 10^{-6}, or the iteration count reaches 400. Algorithm 1 summarizes the trust-region reflective procedure used to solve the D-NLS estimator.

Algorithm 1 Trust-region reflective for D-NLS [45]

Input: $\mathbf{r}(\mathbf{x})$, $\mathbf{lb}, \mathbf{ub}$, initial guesses for $\mathbf{x}$ and Δ
Output: $\mathbf{x}^{(k+1)}$

```
for k = 0, 1, ... do
    Compute r^(k) = r(x^(k)).
    Form J^(k) by forward finite differences in (26)
    Solve s^(k) in (23)
    Compute ρ^(k) according to (27)
    if ρ_k ≥ 0.75 then
        x^(k+1) = x^(k) + s^(k), increase Δ_{k+1}.
    else if ρ_k ≥ 0.25 then
        x^(k+1) = x^(k) + s^(k), keep Δ_{k+1}.
    else
        x^(k+1) = x^(k), reduce Δ_{k+1}.
    end if
    if ||s^(k)||_2 ≤ 10^-6 or ||r^(k)||_2 ≤ 10^-6 or k ≥ 400 then
        break
    end if
end for
```

3) Initialization: The accuracy of the D-NLS estimator is sensitive to the choice of initial parameter guesses. As the estimator employs iterative optimization to minimize measurement residuals, poor initialization may lead to convergence to local minima rather than the global optimum. Owing to the highly nonlinear nature of (19), appropriate parameter initialization is therefore adopted to enhance estimation robustness and accuracy. Since the Doppler multipath error primarily manifests as a high-frequency component, it can be reduced by averaging over a time period. Thus, the initial estimate of the LOS Doppler frequency, $\tilde{f}_{LOS,ini}$, can be approximated as the mean Doppler measurement over an estimation window:

$$\tilde{f}_{LOS,ini} = \frac{1}{M}\sum_{n=1}^{M} f_{0,Rec}(n) \tag{28}$$

Second, as indicated by (19) and the simulation results in Fig. 2, the Doppler oscillation frequency is determined by the period of the trigonometric functions, which in turn is governed by the parameter $\tilde{f}_{shift}$. Consequently, for a Doppler oscillation with a period of P seconds, $\tilde{f}_{shift}$ can be initialized as:

$$\tilde{f}_{shift,ini} = \frac{1}{P} \tag{29}$$

Finally, the amplitude ratio can be initialized using (15) as:

$$\tilde{\alpha}_{ini} = \left| \frac{1 - \frac{\max(\mathbf{f}_{0,Rec}) - \tilde{f}_{LOS,ini}}{\min(\mathbf{f}_{0,Rec}) - \tilde{f}_{LOS,ini}}}{1 + \frac{\max(\mathbf{f}_{0,Rec}) - \tilde{f}_{LOS,ini}}{\min(\mathbf{f}_{0,Rec}) - \tilde{f}_{LOS,ini}}} \right| \tag{30}$$

B. Algorithm design

The overall process for multipath detection and mitigation is outlined in Algorithm 2. Step 3 in Algorithm 2 estimates rough signal parameter ranges based on the

Algorithm 2 Proposed D-NLS estimator for multipath detection and mitigation

Input: The received Doppler measurement consists of K satellites, with Y estimation windows for each channel
Output: The estimated signal parameters $\mathbf{x}$, The multipath indicator

1: **for** $i = 1, 2, ..., K$ **do**
2:     **for** $j = 1, 2, ..., Y$ **do**
3:         Initialize $\mathbf{x}_{ini} = \left[\tilde{f}_{LOS,ini}, \tilde{f}_{shift,ini}, 0, \tilde{\alpha}_{ini}\right]$ based on (28), (29) and (30)
4:         Apply parameter estimation based on Algorithm 1 and get $\mathbf{f}_0(\hat{\mathbf{x}})$ and $\hat{\mathbf{x}}$
5:         **if** $\max\left(\mathbf{f}_0(\hat{\mathbf{x}})\right) - \min\left(\mathbf{f}_0(\hat{\mathbf{x}})\right) > \gamma$ **then**
6:             Add the j-th detection window of i-th satellite to the deterministic multipath subset
7:             Calculate $\hat{f}_{LOS}$ and $\hat{f}_{ref}$ based on (22) and correct receiver Doppler measurement with $\hat{f}_{LOS}$
8:         **end if**
9:     **end for**
10: **end for**
11: Utilize the updated receiver Doppler measurements for navigation

observed Doppler oscillation characteristics. The optimization process can be initialized from multiple starting points, such as through randomized initializations, to improve the likelihood of converging to the global minimum. Step 5 of Algorithm 2 detects multipath by comparing the oscillation range of the estimated Doppler measurement with a predefined threshold. In this work, the threshold is set to 4 Hz, chosen based on the estimator's sensitivity to noise under practical operating conditions. Under LOS conditions, the receiver Doppler measurement contains minimal oscillation, and the estimator modeling Doppler under multipath conditions according to (19). This typically produces either an excessively large amplitude ratio or a near-zero Doppler frequency shift, resulting in an estimated Doppler measurement that is oscillation-free. In contrast, when multipath interference is present, the estimator reconstructs the oscillatory pattern. The accuracy of this reconstruction is essential for reliable multipath detection, as a pronounced oscillation range in the estimated Doppler indicates the presence of multipath. The optimal threshold, however, may depend on specific implementation scenarios. Future work could determine this threshold using data-driven or adaptive methods that account for the statistical characteristics of noise rather than relying on a fixed empirical value.

The derived theoretical models and the signal parameter estimator can also be applied in special cases where the reflected signal is stronger than the direct signal. In such scenarios, the modeling of the estimated receiver Doppler measurement remains similar to (19). However, the definitions of the outputs from the D-NLS estimator differ. Specifically, the estimated $\hat{f}_{LOS}$ represents the Doppler frequency of the reflected signal, while $\hat{f}_{ref}$ corresponds to the desired LOS signal Doppler. Additionally, the estimated $\hat{\alpha}$ indicates the ratio of the reflected signal amplitude to the LOS signal amplitude. The occurrence of this special case can be identified using a pseudorange-based estimator that determines the signal time-of-arrival, along with a consistency check between the pseudorange and Doppler frequency of the signal components. Therefore, this scenario is not well suited to the proposed framework and is not considered further.

The computational complexity of the proposed D-NLS estimator is primarily governed by the trust-region reflective optimization (Algorithm 1). For each estimation window, the nonlinear least squares subproblem involves computing a residual vector of size M and solving a least-squares system using a Jacobian matrix of dimension $M \times 4$, where 4 is the number of signal parameters. The dominant cost of this step scales as $O(4^2 M)$ per iteration, with 4^2 rises from computing the 4×4 matrix $\mathbf{J}^\mathrm{T}\mathbf{J}$. Since 4 is fixed, it is simplified to $O(M)$. Given that Algorithm 1 is invoked for each of the Y estimation windows across K satellite channels, the overall computational complexity of the full estimation process is:

$$O(KYMk_{\max}) \tag{31}$$

where $k_{\max}$ is the number of iterations in Algorithm 1. Therefore, the method scales linearly with the number of satellites, estimation windows, iteration number, and Doppler measurements per window. The experimentally calculated processing time are listed in Table II.

C. Simulation on estimator accuracy

This section evaluates factors that influence estimation accuracy through simulation. First, the CRLB provides the theoretical minimum variance for any unbiased estimator and is derived from the inverse of the Fisher information matrix (FIM) [46]. For instance, the FIM for the parameter $\tilde{f}_{LOS}$ is given by:

$$FIM(\tilde{f}_{LOS}) = -E\left[\frac{\partial^2 \ln p\left(\mathbf{f}_{0,Rec};\mathbf{x}\right)}{\partial \tilde{f}_{LOS}^2}\right] \tag{32}$$

where $p\left(\mathbf{f}_{0,Rec};\mathbf{x}\right)$ denotes the likelihood function of the receiver Doppler frequencies given $\mathbf{x}$, expressed as:

$$p\left(\mathbf{f}_{0,Rec};\mathbf{x}\right) = \left(2\pi\sigma^2\right)^{-\frac{M}{2}} \exp\left[-\frac{1}{2\sigma^2}\sum_{n=1}^{M}\left(f_{0,Rec}\left(n\right) - \tilde{f}_0\left(n;\mathbf{x}\right)\right)^2\right] \tag{33}$$

Assuming white Gaussian noise in the receiver Doppler measurement, and σ^2 is the noise variance. Therefore, CRLB for $\tilde{f}_{LOS}$ is given by:

$$\mathrm{CRLB}\left(\tilde{f}_{LOS}\right) = FIM(\tilde{f}_{LOS})^{-1} = \frac{\sigma^2}{M} \tag{34}$$

The CRLBs for the remaining three parameters are computed using numerical approximation. The CRLBs can be derived by approximating the partial derivatives of the signal model with respect to the unknown parameters. For instance, the partial derivative of the signal model with respect to a parameter x_i is given by:

$$\frac{\partial \tilde{f}_0\left(n;\mathbf{x}\right)}{\partial x_i} \approx \frac{\tilde{f}_0\left(n;x_i+\varepsilon\mathbf{e}_i\right) - \tilde{f}_0\left(n;x_i\right)}{\varepsilon} \tag{35}$$

It is mathematically equivalent to the Jacobian computation in (26). The Jacobian matrix quantifies how small changes in the parameters affect the model output, making it a direct measure of the estimator's sensitivity. This sensitivity, in turn, determines the amount of Fisher information and thus influences the CRLB. The corresponding element of the FIM is then computed as [46]:

$$FIM_{ij} = \frac{1}{\sigma^2}\sum_{n=1}^{M}\frac{\partial \mathbf{f}_0\left(n;\mathbf{x}\right)}{\partial x_i}\frac{\partial \mathbf{f}_0\left(n;\mathbf{x}\right)}{\partial x_j} \tag{36}$$

Second, simulations are conducted to assess the performance of the proposed D-NLS estimator, focusing on two key factors: noise variance and measurement sample size. Doppler measurement noise $v_{mea}(n)$ is primarily attributed to thermal noise, and its standard deviation is simulated based on the 1-sigma frequency jitter as [1]:

$$\sigma = \frac{1}{2\pi T}\sqrt{\frac{4FB_n}{C/N_0}\left(1+\frac{1}{TC/N_0}\right)} \tag{37}$$

where

$$
\begin{aligned}
F &= 1 \text{ at high } C/N_0 \\
&= 2 \text{ near threshold} \\
B_n &= \text{Noise Bandwidth (Hz)}
\end{aligned}
$$

C/N_0 represents the strength of the received compound signal. Using the derived model, the receiver Doppler measurement under multipath interference is simulated for predefined signal parameters and impact factor settings. Parameter estimation is performed with Algorithm 2, and for each impact factor setting, 5000 Monte-Carlo trials are run to compute the root mean square error (RMSE), which is then compared with the corresponding CRLB. Throughout the simulations, the parameters of the direct and reflected signals, as well as the receiver settings, are kept constant, as specified in Table I.

TABLE I
Simulation parameter settings

f_{LOS}	f_{shift}	$\Delta\phi_{shift}$	α	T	B_n
0 Hz	15 Hz	0 degree	2	1 ms	20 Hz

The impact of noise is analyzed with a fixed measurement sample size of 300 milliseconds (ms). Fig. 5 (a) presents the simulation and theoretical parameter estimation accuracy across varying C/N_0. An increase in C/N_0 reduces the noise impact on the receiver Doppler measurement, making the Doppler oscillation feature more distinct and improving the accuracy of parameter estimation. Compared with $\tilde{f}_{shift}$, $\tilde{f}_{LOS}$ has a higher CRLB, indicating a theoretically lower estimation accuracy. However, its estimation performance closely approaches the CRLB, suggesting that the proposed algorithm operates near optimally for $\tilde{f}_{LOS}$. The parameters $\tilde{f}_{shift}$, $\Delta\tilde{\phi}_{shift}$, and $\tilde{\alpha}$ exhibit similar CRLBs as they are mainly influenced by the Doppler oscillation. For low C/N_0 values, extremely high noise interferes with the initial guess process in the algorithm, preventing the estimator from converging properly. However, since these parameters are constrained by fixed boundaries, where $\tilde{\alpha}$ is limited to $[1, 30]$ and $\Delta\tilde{\phi}_{shift}$ is constrained by $[-\pi, \pi]$, their estimated values remain artificially within these bounds. As C/N_0 increases beyond approximately 30 dB-Hz, the discrepancy between simulation and CRLB diminishes. However, estimation accuracy of $\tilde{f}_{shift}$ still has room for improvement. Future enhancements could focus on developing a more robust algorithm with noise filtering techniques to reduce sensitivity to noise and outliers.

The impact of the sample size on the estimator is evaluated with a fixed C/N_0 of 40 dB-Hz. As shown in Fig. 5 (b), the estimator accuracy improves with increasing sample size, with acceptable performance for sample sizes greater than 120 ms. However, as the sample size exceeds 300 ms, the estimator error gradually increases, deviating from the CRLB. This occurs because the proposed D-NLS method does not explicitly account for noise distribution or variance, and increasing the number of measurements introduces more noise, causing the estimator to fit to these noisy deviations. Additionally, the highly nonlinear nature of the Doppler measurement model means that too large a sample size does not necessarily improve accuracy, as the estimator becomes invalid over larger regions of the parameter space. When the sample size is too small, the numerically simulated CRLBs appear to be too large. In conclusion, the proposed estimator performs well in high C/N_0 and moderate sample size scenarios.

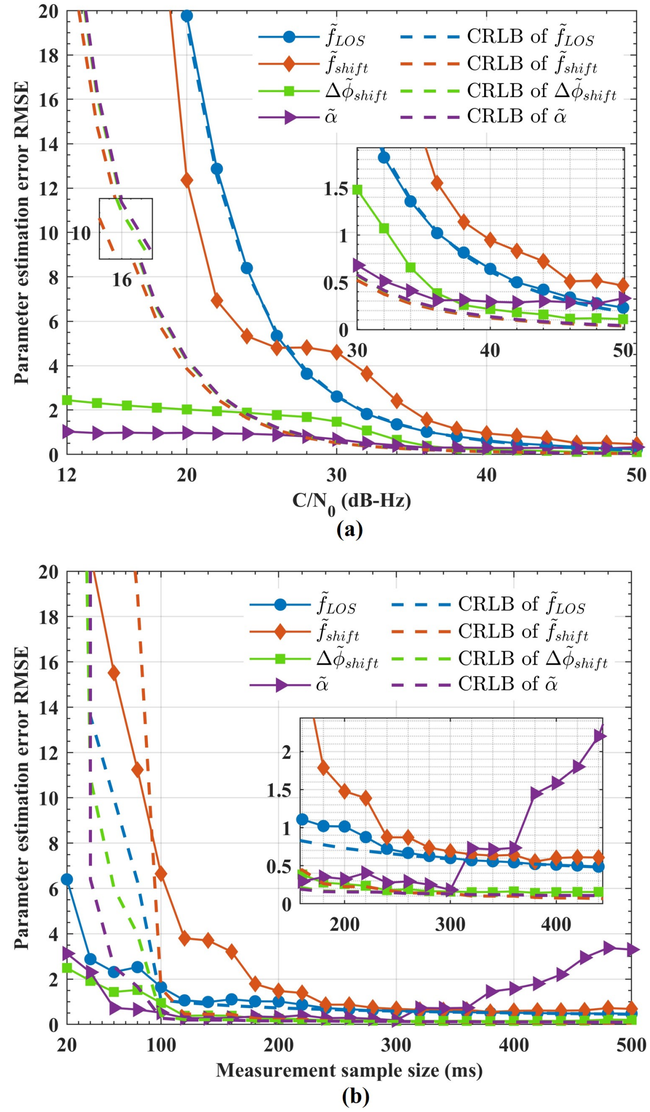

Fig. 5. Plots of the RMSEs and CRLBs for the LOS signal's Doppler frequency (Hz), Doppler frequency shift of the reflected signal (Hz), initial carrier phase shift (radians), and signal amplitude ratio, varying with (a) C/N_0 values and (b) measurement sample size.

IV. EXPERIMENTS

To investigate both the fundamental characteristics of multipath-induced Doppler errors and the robustness of the proposed mitigation method, two experimental scenarios are presented. In scenario 1, a pedestrian walks perpendicular to a building surface, as indicated by the red arrow in Fig. 6 (a), allowing for multipath reception from the south. This controlled setup creates a well-defined reflected path geometry and induces a varying Doppler shift in the reflected signals, enabling theoretical validation and baseline performance evaluation of the proposed algorithm. The pedestrian carries a backpack equipped with test devices, as shown in Fig. 6 (b). A LABSAT 3 Wideband (3W) system records GPS L1 intermediate frequency (IF) data for post-processing using a GNSS software-defined receiver (SDR), while a NovAtel SPAN-CPT system, connected via a splitter to the same antenna, provides centimeter-level ground truth for validation [47, 48]. Scenario 2 extends the evaluation to a vehicle navigating a dense urban canyon (Fig. 6 (c)), characterized by rapidly changing satellite-receiver dynamics and time-varying multipath. Although the presence of multipath is often brief and localized in such scenarios, it offers a realistic assessment of the algorithm's operational performance. The same test devices are shown in Fig. 6 (d), and are installed in the vehicle for consistency across scenarios.

The sky plots categorize satellites into LOS and multipath types based on ray-tracing analysis. The ray-tracing algorithm [36], which incorporates satellite ephemeris, the 3D building model, and user PVT data, estimates the most probable signal propagation paths. The ray-tracing model assumes perfect specular reflections from building surfaces, and a satellite is classified as experiencing multipath interference if more than one satellite-receiver path is identified. The ray-tracing result indicates that for scenario 1, PRN 22 is geometrically susceptible to multipath effects throughout the test, while PRN 5 experiences multipath interference over several epochs. For scenario 2, around 10 seconds of signal from PRN 15 are classified as multipath. Therefore, the subsequent analysis focuses on PRN 22 of scenario 1 and PRN 15 of scenario 2, which exhibit the highest likelihood of sustained multipath interference.

In the GNSS SDR implementation, the coherent integration time is set to 1 ms. The PLL loop bandwidth is set to 20 Hz for pedestrian tests and 40 Hz for vehicular tests, while the D-NLS method processes a 300 ms sample window for each estimation. Table II summarizes the computational environment and measured runtime of the proposed D-NLS estimator implemented in MATLAB. Under the same hardware configuration, the processing time required for the correlation stage in MEDLL is also reported and will be discussed in detail in Section IV.B. Here, F_s, B, K, C, and T denote the sampling frequency, the front-end bandwidth, the number of satellites, the number of correlators, and the coherent integration time, respectively. The GPS IF data and ground truth have been open-sourced on GitHub at: https://github.com/Fangjingxiaotao/GNSS-OpenIF.

TABLE II
System configuration and processing time

Item	Value
CPU	Intel i9-12900K, 3.19 GHz
RAM	32 GB
Operating system	Windows 11 Pro
MATLAB	R2024a
GPS IF data	$F_s = 58\,\text{MHz},\ B = 56\,\text{MHz}$
D-NLS	
Algorithm parameters	$K = 6,\ Y = 3.33,\ M = 300,\ k_{\max} \approx 16$
Mean proc. time (1 s GNSS)	1.38 s
MEDLL	
Algorithm parameters	$K = 6,\ C = 161,\ T = 1\,\text{ms}$
Mean proc. time (1 s GNSS)	440 s

A. The proposed parameter estimator performance

1) Scenario 1: The *receiver Doppler measurements* correspond to the nominal GNSS receiver outputs obtained from the GNSS SDR after PLL filtering. Fig. 7 (a) presents the receiver Doppler measurements of PRN 22 of scenario 1. Fig. 7 (b) illustrates the corresponding true velocity of the pedestrian. The pedestrian remains stationary for approximately 15 seconds before engaging in a repeated reciprocating motion. The Doppler frequency exhibits periodic variations corresponding to velocity variations during the reciprocating movement. The subfigures in Fig. 7 (a) provide a detailed view of the Doppler performance at approximately 48 and 53 s, respectively. Notably, the Doppler measurement demonstrates distinct high-frequency oscillations with a prolonged upward or downward tail. This observed Doppler oscillation feature closely resembles the theoretical multipath-induced Doppler oscillation simulated in Fig. 2.

The receiver Doppler measurement is input to the D-NLS estimator, and the parameter estimation performance is presented in Fig. 8. Fig. 8 (b) and (c) provide zoomed-in views at approximately 48 and 53 seconds, respectively. The *received Doppler* is the receiver Doppler measurement from the GNSS receiver. The *estimated Doppler* represents the estimation output from D-NLS, showing strong consistency with the received Doppler across multiple epochs, validating the effectiveness of the proposed estimator in capturing the multipath-induced oscillation feature. The estimated Doppler frequency of the LOS signal follows the variations in the receiver Doppler measurement, while the estimated Doppler frequency of the reflected signal exhibits an inverse pattern. In certain epochs, the Doppler difference between the LOS and reflected signals reaches 20 Hz. This is because the reflected signal path changes perpendicularly to the building surface, altering the velocity projection along the LOS and reflected signal paths in different directions. Consequently, the Doppler difference between the LOS and reflected signals exists. In Fig. 8 (b), the estimated Doppler frequency of the reflected signal is approximately 15 Hz lower than that of the LOS signal, whereas in Fig. 8 (c), the reflected signal exhibits a higher Doppler

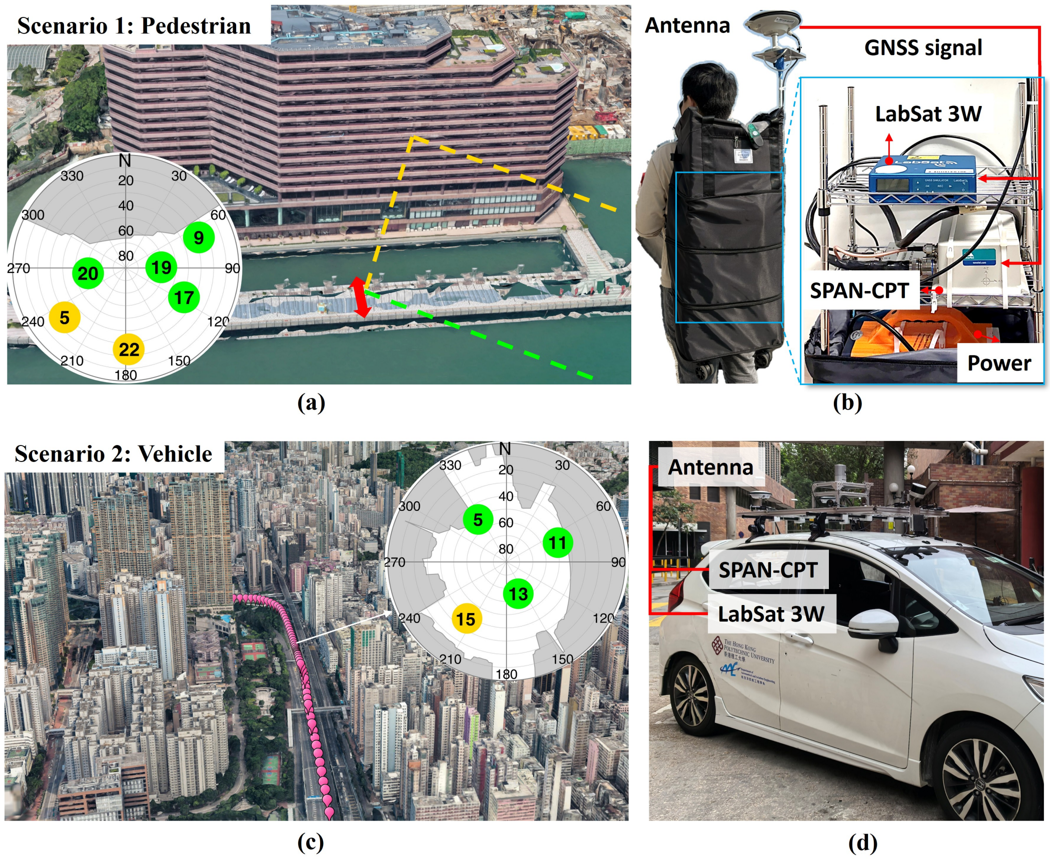

Fig. 6. (a) Test environment in scenario 1, showing the test trajectory (red arrow) and sky plot and (b) equipment setup in scenario 1. (c) Test environment in scenario 2, showing the test trajectory (pink icons) and sky plot in 35 seconds and (d) equipment setup in scenario 2. Satellites in green indicate LOS signals, while those in orange represent multipath interference based on ray-tracing analysis.

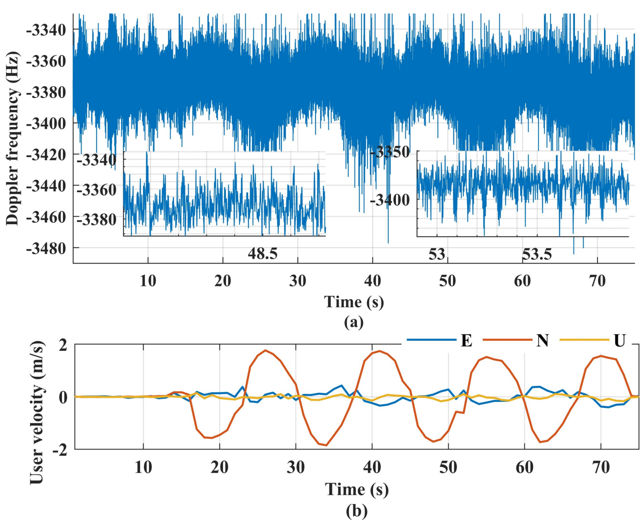

Fig. 7. (a) Doppler measurement of PRN 22 of scenario 1 obtained from the GNSS SDR. (b) True user velocity recorded by the SPAN-CPT system.

frequency. This is attributed to the reversal of the user's velocity direction between the two cases. In addition, the oscillation period is measured to be approximately 76 ms, corresponding to a $\tilde{f}_{shift,ini}$ of around 13 Hz, as derived from (29), which closely aligns with the optimal estimation results.

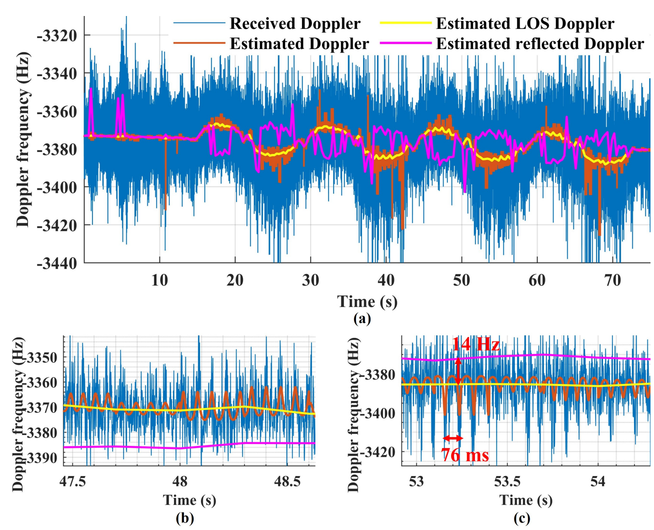

Fig. 8. (a) Overview of the D-NLS estimator performance for PRN 22 of scenario 1. (b) Zoomed-in view at approximately 48 seconds. (c) Zoomed-in view at approximately 53 seconds.

Fig. 9 presents the performance of the proposed D-NLS estimator for PRN 17 in a LOS reception scenario. The results indicate that the estimated Doppler remains flat, with the estimated Doppler frequencies of the LOS and reflected signals nearly overlapping. This outcome is expected, as the absence of Doppler oscillation features causes the estimator to stabilize, fitting the noise optimally. This behavior aligns with the theoretical analysis in Section III. B. However, in certain epochs, a high-frequency shift of the reflected signal is estimated, possibly leading to false alarms in the proposed detector. To mitigate this, more advanced estimation algorithms that account for noise distributions and incorporate outlier detection may be required to enhance the robustness and accuracy of Doppler oscillation feature matching.

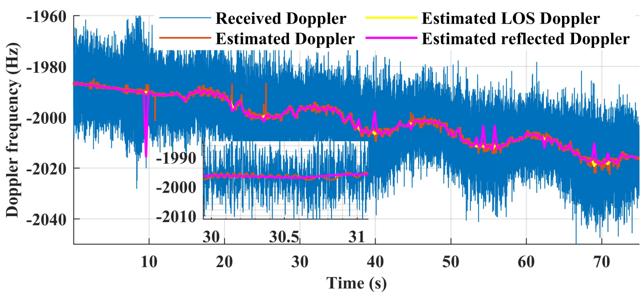

Fig. 9. D-NLS estimator performance for PRN 17 of scenario 1.

The ray-tracing algorithm utilizes ground truth PVT information from the SPAN-CPT, satellite ephemeris, and the 3D building model to determine the most possible signal propagation paths and compute the corresponding Doppler frequency for each signal ray. The ray-tracing simulated Doppler frequencies remain unaffected by GNSS-related interference, including noise, multipath effects, and atmospheric disturbances. Therefore, the ray-tracing simulated Doppler frequencies are considered the true Doppler values. Since receiver clock errors affect all satellites uniformly within the same test, the single-difference Doppler frequency is computed to mitigate the impact of receiver clock drift on Doppler measurements. The single-difference Doppler frequency is defined as the Doppler difference between a test satellite and a reference satellite that receives only a LOS signal, expressed as:

$$f_{single} = f_{test} - f_{refer} \tag{38}$$

Thus, the single-difference Doppler frequency retains the multipath-induced error from the test satellite. In this analysis, PRN 22 is selected as the test satellite, while PRN 20 serves as the reference satellite. Fig. 10 presents a comparison between the estimated Doppler frequencies and the true Doppler frequencies simulated by the ray-tracing technique for PRN 22. The estimated LOS Doppler closely aligns with the true values throughout the test, demonstrating the accuracy of the proposed method. The estimated reflected Doppler also exhibits satisfactory accuracy, although occasional outliers are expected. As shown in Fig. 5, the simulated RMSE of $\tilde{f}_{shift}$ is higher than that of $\tilde{f}_{LOS}$ under the considered C/N_0 and sample size. Because the reflected signal is weaker, its Doppler estimate is more susceptible to noise and receiver dynamics. The dominance of the stronger LOS component is also evident in Fig. 2 (a). The RMSE for the estimation of LOS Doppler and reflected Doppler is 2 Hz and 6 Hz, respectively.

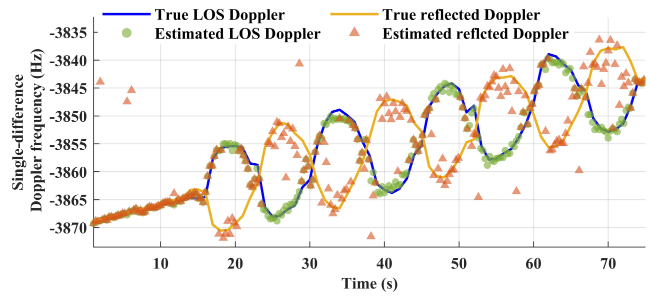

Fig. 10. Comparison of the estimated Doppler frequencies obtained using the proposed method with the true Doppler frequencies simulated by the ray-tracing technique. PRN 22 of scenario 1 serves as the test satellite, while PRN 20 of scenario 1 is used as the reference satellite for single-difference Doppler calculation.

2) Scenario 2: Fig. 11 (a) presents the parameter estimation performance of PRN 15. Strong oscillatory behavior is observed in the Doppler measurements in Fig. 11 (b). At around 36 seconds, the oscillation period is approximately 45 ms, and the frequency shift of the reflected signal is estimated to be around 25 Hz, corresponding to a vehicle speed of about 5 m/s. After around 50 seconds, the receiver loses lock on the signal, likely due to signal blockage. Measurements from around 31 to 45 seconds are classified as under multipath interference according to ray-tracing. As shown in Fig. 11 (c), the green diamonds represent reflection points determined via ray-tracing, while the blue dots indicate the vehicle's trajectory. The reflection points are concentrated around the surface of a glass-curtain high-rise building, confirming the physical plausibility of the detected multipath. Compared with the pedestrian scenario (Scenario 1), the increased user velocity in this vehicular setting leads to a larger Doppler shift in the reflected signal, which enhances observability but also introduces challenges. Specifically, the high dynamics result in noisier Doppler measurements and reduced tracking stability, making it more difficult for the estimator to maintain robust and consistent performance throughout the entire period.

Fig. 12 compares the single-difference Doppler frequencies produced by the proposed D-NLS estimator with the ray-tracing ground truth for PRN 15 in scenario 2. Due to the high mobility of the vehicle, PRN 15 is susceptible to multipath interference only between 31 and 45 seconds. In this interval, the estimated reflected Doppler matches the ray-tracing-based ground truth, demonstrating the potential of the proposed method in urban vehicular scenarios. Outside this interval, some inconsistencies appear between the estimator and the ray-tracing labels. Four representative cases are enclosed by dashed boxes in Fig. 12 and analyzed in detail in Fig. 13.

Fig. 13 presents four magnified time windows, each spanning approximately 0.4 seconds, illustrating conditions where the D-NLS estimator and the ray-tracing

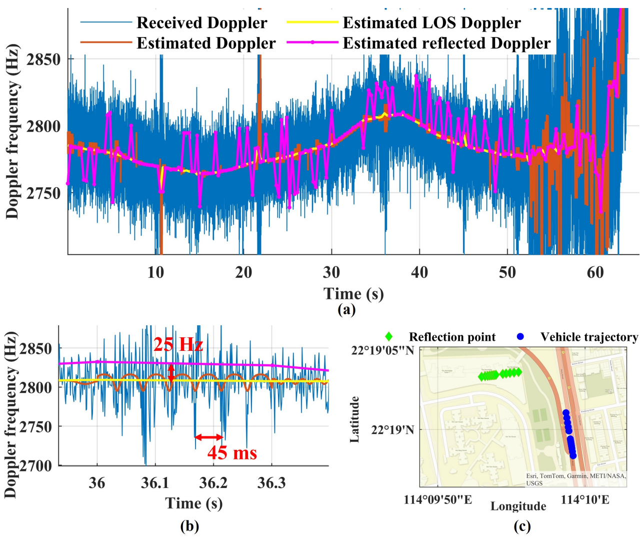

Fig. 11. (a) Overview of the D-NLS estimator performance for PRN 15 of scenario 2. (b) Zoomed-in view at approximately 36 seconds. (c) The vehicle trajectory and reflection point locations of PRN 15 from around 31 to 45 seconds.

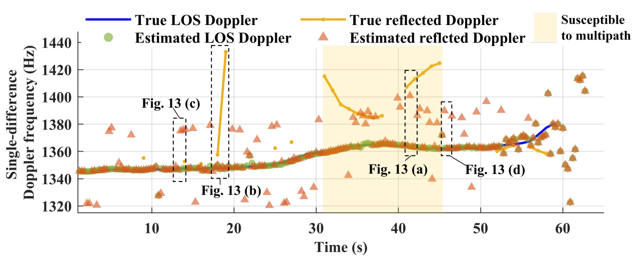

Fig. 12. Comparison of the estimated Doppler frequencies obtained using the proposed method with the true Doppler frequencies simulated by the ray-tracing technique. PRN 15 of scenario 2 serves as the test satellite, while PRN 13 of scenario 2 is used as the reference satellite for single-difference Doppler calculation.

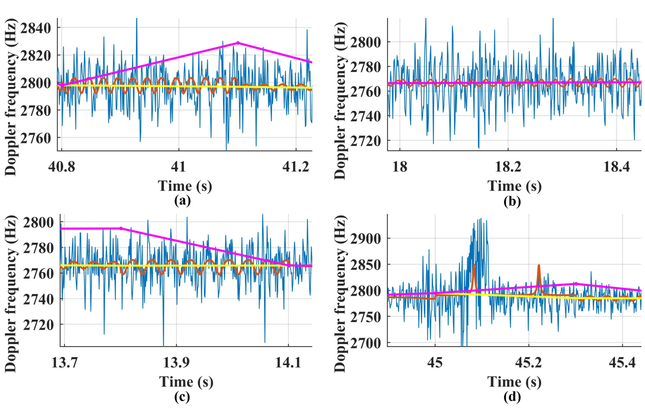

Fig. 13. Zoomed-in views of the D-NLS estimator performance for PRN 15 in scenario 2, illustrating inconsistency cases arising from: (a) estimation gap between D-NLS and ray-tracing; (b) ray-tracing false alarms; (c) missed detections in ray-tracing; and (d) false alarms in the D-NLS estimator.

reference diverge. Fig. 13 (a): At around 41 seconds, the two methods differ by around 10 Hz according to Fig. 12. This does not necessarily indicate the D-NLS estimator failure, as the D-NLS output aligns well with the observed Doppler oscillation. Moreover, ray-tracing, which relies on simplified geometric optics, cannot fully account for effects induced by irregular building geometries, vegetation, or dynamic occlusions [36, 49]. Fig. 13 (b): Ray-tracing detects a multipath event at around 18 seconds, whereas the D-NLS estimator does not. This discrepancy may result from a ray-tracing false alarm or from Doppler oscillation features too weak to emerge from noise. Fig. 13 (c): The D-NLS estimator detects multipath-induced Doppler oscillation, but the ray-tracing method remains silent, possibly due to the limited precision in its 3D building model. Fig. 13 (d): The D-NLS estimator generates a false alarm by misinterpreting noise-induced or dynamically unstable tracking fluctuations as multipath. These observations indicate that both the D-NLS estimator and the ray-tracing technique face challenges in maintaining robustness under highly dynamic and noisy conditions. Future improvements may be achieved through enhanced noise-filtering and outlier-detection strategies.

In conclusion, the proposed estimator demonstrates satisfactory accuracy and robustness in the pedestrian scenario, as well as a promising capability for estimation in high-dynamic vehicular environments. The results also reveal several key limitations of this method. First, its effectiveness is primarily constrained to dynamic user scenarios. Second, the impact of noise on practical FLL tracking accuracy is not accounted for, which may affect estimation precision. Improved accuracy could be achieved by incorporating a posterior noise model in the Doppler measurement. Lastly, the proposed model is limited to multipath scenarios involving two incoming signals where LOS remains dominant. In more complex cases with multiple reflected signals within a single channel, the accuracy of signal parameter estimation may be compromised.

B. Comparison

The accuracy of the parameter amplitude ratio is verified by comparing it with the widely recognized correlator-based parametric method, MEDLL, using scenario 1 data. Originally proposed by Van Nee [11], MEDLL is frequently employed as a benchmark for multipath parameter estimation, particularly under mild multipath conditions [50]. The purpose of this comparison is to highlight the relative strengths, operational properties, and limitations of each method under realistic multipath conditions.

Recognizing that the performance of MEDLL significantly depends on its correlator configuration, this work implemented a high-performance version to ensure a robust comparison with our proposed estimator. Specifically, the search region is set to ± 2 chips, with a correlator spacing of 0.025 chips, resulting in a total of 161 correlators. The coherent integration time and estimation window size are configured identically to the D-NLS algorithm, meaning that 300 ms of correlator outputs are averaged for each MEDLL estimation. According to Table II, the processing time for a single correlation in MEDLL is approximately 0.46 ms, which is comparable to the values reported in [51, 52]. MEDLL estimates parameters such as code delay, amplitude ratio, and initial carrier phase shift between the LOS and reflected signals. The estimated amplitude ratio is used for direct comparison, while the estimated code delay is analyzed to assess MEDLL's effectiveness in parameter estimation. The carrier phase error is not discussed due to its rapid variations caused by the integer ambiguities and cycle slips in the stand-alone receiver.

Fig. 14 (a) presents the amplitude ratio between LOS and reflected signals as estimated by both the D-NLS and MEDLL algorithms for PRN 22. The shaded areas indicate user movement, referring to the user velocity in Fig. 7 (b). Short static periods occur due to changes in movement direction during the user's reciprocating motion. Determining true amplitude ratios from real data is challenging, as reflected signal power depends on unknown reflector materials and environmental noise. Studies report that reflected signals in urban GNSS environments typically experience 5-20 dB attenuation relative to the LOS component [53, 54]. Therefore, a reference amplitude ratio threshold is included in the plot to help assess the realism of the estimated values. An amplitude ratio greater than 10 suggests that the reflected signal has a C/N_0 approximately 20 dB lower than the LOS signal, implying minimal or undetectable multipath interference.

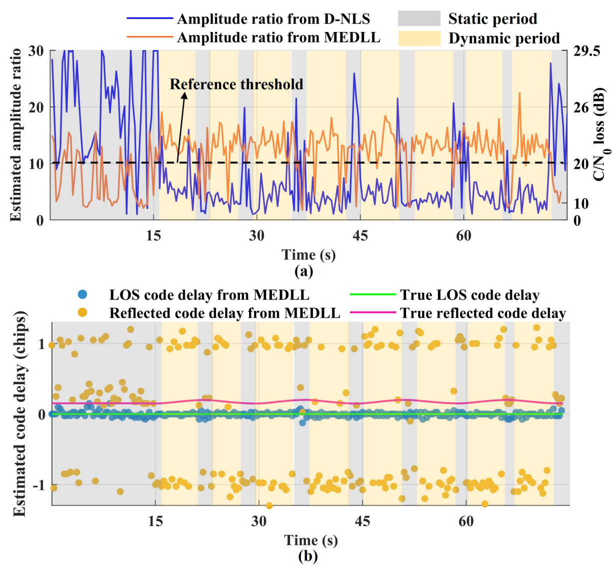

Fig. 14. (a) Comparison of amplitude ratio (C/N_0 loss of reflected signal) estimation between the proposed D-NLS and MEDLL for PRN 22 of scenario 1. (b) Code delay estimation results from MEDLL and true code delays simulated by ray-tracing, for PRN 22 of scenario 1. The gray-shaded area indicates the user-static period, and the orange-shaded area represents the user-dynamic period.

During static periods, the D-NLS algorithm shows limited performance, while the MEDLL amplitude ratio output remains between 2 and 4 for several epochs. An amplitude ratio of 2 to 4 corresponds to a reflected signal power loss of approximately 6 to 12 dB, which is realistic in real-world applications. When the user is dynamic, the D-NLS estimated amplitude ratio ranges from 2 to 5, while MEDLL shows unreliable estimation. Fig. 14 (b) presents the code delay estimation from MEDLL alongside the true signal code delays provided by the ray-tracing algorithm. The LOS signal code delay is consistently estimated to be around zero, which aligns with expectations. During the static period, the estimated code delay for the reflected signal remains stable at approximately 0.2 chips in a few epochs, indicating that MEDLL successfully detects multipath and estimates the signal parameters. However, during the dynamic period, the estimated code delay exhibits rapid fluctuations, likely due to the ACF feature of multipath being masked by noise. This instability suggests a failure of convergence in multipath parameter estimation.

Table III summarizes the characteristics of the traditional MEDLL and the proposed D-NLS methods. The results suggest that both methods provide reasonable estimation and multipath detection, but under different user dynamics. Therefore, combining the two methods is advantageous, allowing for greater adaptability in a wider range of applications. The combination method can also refer to the PR and PR rate envelopes described in Section II. C.

The following section compares the multipath detection performance of the proposed D-NLS method, MEDLL, and SQM metrics, including the delta test and the (single-sided) ratio test. The detection threshold for the D-NLS detector (γ) is set to 4 Hz. The multipath detection performance of the D-NLS method can be visually verified from Fig. 8 (a). Specifically, intervals where the estimated reflected Doppler notably deviates from the stable LOS Doppler, resulting in significant Doppler oscillations, correspond directly to successful multipath detection events. According to the MEDLL performance example shown in Fig. 14, multipath detection in MEDLL is empirically configured based on the estimated amplitude ratio and code delay. A multipath alarm is triggered when the estimated amplitude ratio is below 13, and the estimated code delay of the reflected signal lies within the interval $(-1, 1)$ chips. Multipath interference affects SQM metric statistics (e.g., mean and variance), and it is detected when these metrics deviate from their nominal values, as detailed in [16]. The threshold is calculated based on the signal's C/N_0, with a false alarm probability set to 1%. The detector sample size is set to 300 ms, consistent with the proposed method. The performance of the delta and ratio metrics on PRNs 17 and 22 is shown in Fig. 15.

The multipath detection rate is determined as the ratio of detected epochs to the total number of epochs. For satellites under LOS conditions, this rate represents the

TABLE III

Characteristics of the proposed D-NLS method and the typical MEDLL method

	D-NLS	MEDLL [15, 11]
Input	Doppler measurement	Correlator values
Output	Doppler frequencies, carrier phase errors, amplitudes of signal components	Code delays, carrier phase errors, amplitudes of signal components
Additional receiver configuration	No	Multiple correlators
Limitation	Only work in dynamic users; Only work in one LOS + one reflected (attenuated) cases	High computational burden; Sensitive to noise and user dynamics
Feature	Higher Doppler resolution improves performance	Higher correlator resolution improves performance

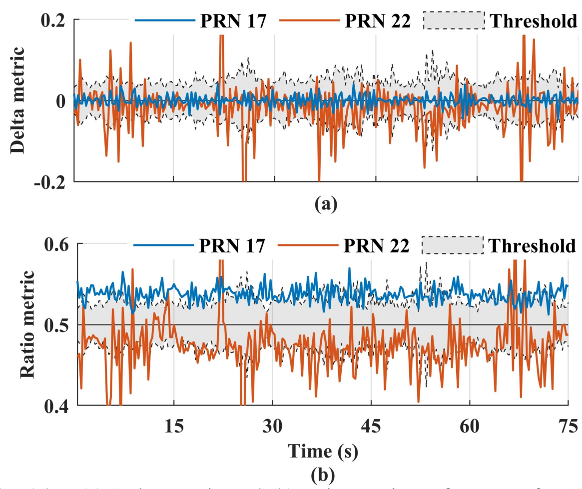

Fig. 15. (a) Delta metric and (b) ratio metric performance for PRN 17 (LOS) and PRN 22 (multipath) of scenario 1, respectively.

false alarm rate, whereas for satellites affected by multipath, it corresponds to the correct detection rate. Table IV summarizes the multipath detection rates of the methods for all observed satellites. The satellites are ordered based on signal power, with PRN 20 having the strongest signal and PRN 22 the weakest. All four methods indicate a high

TABLE IV

Detection rates for the D-NLS method, MEDLL algorithm, delta metric, and ratio metric for all satellites. PRNs 5 and 22 of scenario 1 are classified as multipath-type satellites.

Detection rate\PRN	20	19	17	5	9	22
D-NLS (%)	1.2	0.8	4.8	14	12	50.8
MEDLL (%)	0	0	6.5	11.3	0	41.7
Delta test (%)	1.6	1.2	6	11.6	10.8	27.2
Ratio test (%)	7.2	5.6	93.6	24	12.8	44

likelihood that PRN 22 is affected by multipath, consistent with the ray-tracing classification results. While the ratio test achieves an acceptable detection rate for PRN 22, it exhibits a high false alarm rate for LOS satellites due to its sensitivity to ACF distortion. The proposed D-NLS detector achieves a 51% detection rate for PRN 22, which increases to 64% when considering only user dynamic epochs. For PRN 5, the D-NLS, MEDLL, and delta metrics demonstrate a higher detection rate than those observed for LOS satellites. These results suggest that, compared to traditional detectors, the proposed D-NLS method offers high sensitivity to multipath interference while maintaining a low false alarm rate for LOS reception.

V. CONCLUSION

Multipath interference represents one of the primary error sources in GNSS positioning. This study derives a theoretical Doppler measurement model by analyzing error propagation in the receiver's FLL and identifies a Doppler oscillation phenomenon induced by multipath interference. A Doppler-based signal multipath parameter estimation method is proposed, leveraging Doppler oscillation features for multipath detection and mitigation. The estimator, implemented using a nonlinear least squares algorithm, estimates the Doppler frequency difference, carrier phase difference, and signal strength difference between LOS and reflected signals. The proposed D-NLS estimator is evaluated using real-world pedestrian and vehicle tests conducted in urban areas, with its estimation accuracy validated against ray-tracing simulations. Results indicate that the estimated Doppler oscillation closely aligns with measured Doppler performance under multipath conditions. The estimated Doppler frequencies of the LOS and reflected signals show satisfactory consistency with those simulated via ray-tracing. Compared to the MEDLL algorithm, the D-NLS method demonstrates better estimation accuracy in dynamic scenarios, whereas MEDLL remains more effective in static cases. Comparative analysis with traditional SQM metrics, including delta and ratio metrics, shows that the D-NLS method achieves a multipath detection rate of approximately 64% in dynamic scenarios while maintaining a low false alarm rate.

The proposed Doppler-based parameter estimation method shows considerable potential for further enhancement in estimation accuracy and robustness against interferences from receiver dynamics and noise. Future research could explore more advanced estimators or machine learning-based techniques to meet the demands of commercial applications, such as scenarios involving multiple reflections. Additionally, this study highlights the reliability and effectiveness of Doppler measurements for multipath detection and parameter estimation. Future work should focus on integrating corrected Doppler frequencies into receiver frequency and code tracking loops to enhance overall navigation performance.

APPENDIX

A. Deviation of receiver Doppler measurement model

Although the Doppler measurement in (13) is defined in discrete epoch ($t_n = t_0 + nT$), the derivations in appendixes are carried out in continuous time and evaluated at $t = t_n$. Hence, the sampled value of any continuous-time quantity $g(t)$ at t_n is denoted by $g(n) \triangleq g(t_n)$. (13) can be approximated by taking derivative over time as:

$$f_0(n) \approx f_{LOS}(n) + \left.\frac{\partial \Delta\phi_{MP}(n)}{2\pi\partial t}\right|_{t=t_n} \tag{A.1}$$

According to (10),

$$\left.\frac{\partial \Delta\phi_{MP}(n)}{2\pi\partial t}\right|_{t=t_n} = \left.\frac{\partial}{2\pi\partial t}\arctan\left(\frac{\sin\left(\Delta\phi_{ref}(n) - \Delta\phi_{LOS}(n)\right)}{\alpha(n) + \cos\left(\Delta\phi_{ref}(n) - \Delta\phi_{LOS}(n)\right)}\right)\right|_{t=t_n} \tag{A.2}$$

Let variable x written as:

$$\begin{aligned} x &= \Delta\phi_{ref}(n) - \Delta\phi_{LOS}(n) \\ &= \int_{t_0}^{t_n} 2\pi\left(f_{ref}(\tau) - f_{LOS}(\tau)\right)d\tau \\ &+ \Delta\phi_{ref}(t_0) - \Delta\phi_{LOS}(t_0) \end{aligned} \tag{A.3}$$

Let variable y represents:

$$y = \Delta\phi_{MP}(n) = \arctan\left(u(x)\right) \tag{A.4}$$

where

$$u(x) = \frac{\sin(x)}{\alpha(n) + \cos(x)} \tag{A.5}$$

Then the chain rule gives:

$$\begin{aligned} \frac{\partial y}{\partial x} &= \frac{1}{1+u(x)^2}\cdot\frac{\partial u}{\partial x} \\ &= \frac{\alpha(n)\cos(x)+1}{\alpha^2(n) + 2\alpha(n)\cos(x) + 1} \end{aligned} \tag{A.6}$$

According to (A.3), get

$$\begin{aligned} \left.\frac{\partial x}{\partial t}\right|_{t=t_n} &= 2\pi\left(f_{ref}(t_n) - f_{LOS}(t_n)\right) \\ &\triangleq 2\pi\left(f_{ref}(n) - f_{LOS}(n)\right) \end{aligned} \tag{A.7}$$

The amplitude ratio $\alpha(n)$ is assumed to be constant within one epoch. Therefore, the component of the Doppler multipath error can be written as:

$$\begin{aligned} \left.\frac{\partial \Delta\phi_{MP}(n)}{2\pi\partial t}\right|_{t=t_n} &= \left.\frac{1}{2\pi}\frac{\partial y}{\partial x}\frac{\partial x}{\partial t}\right|_{t=t_n} \\ &= \left(f_{ref}(n) - f_{LOS}(n)\right)\left(\frac{\alpha(n)\cos(x)+1}{\alpha^2(n) + 2\alpha(n)\cos(x)+1}\right) \end{aligned} \tag{A.8}$$

Finally, without loss of generality, the receiver Doppler measurement model is transformed as (A.9)

B. The maximum and minimum Doppler multipath errors

According to (14), the Doppler multipath error is model as

$$f_{MP}(n) = f_{shift}(n)\cdot\left(\frac{\alpha(n)\cos(x)+1}{\alpha^2(n) + 2\alpha(n)\cos(x)+1}\right) \tag{B.1}$$

where $x = \int_{t_0}^{t_n} 2\pi f_{shift}(\tau)d\tau + \Delta\phi_{shift}(t_0)$. The continuous-time notation in Appendix A is adopted here and the sampled value of any continuous-time quantity $g(t)$ at t_n is denoted by $g(n)$. For each epoch, α and f_{shift} are treated as constants when taking time derivatives. Take derivative of f_{MP} over t, get

$$\begin{aligned} \left.\frac{\partial f_{MP}(n)}{\partial t}\right|_{t=t_n} &= \left.\frac{\partial f_{MP}(n)}{\partial x}\frac{\partial x}{\partial t}\right|_{t=t_n} \\ &= 2\pi f_{shift}^2(n)\cdot\frac{\alpha(n)\sin x - \alpha^3(n)\sin x}{\left(1+2\alpha(n)\cos x + \alpha^2(n)\right)^2} \end{aligned} \tag{B.2}$$

The extreme points of $f_{MP}(n)$ exist when $\frac{\partial f_{MP}(n)}{\partial t} = 0$. Therefore, the maximum and minimum Doppler multipath error occurs when $\sin x = 0$ or equivalently $\cos x = \pm 1$. For example when $\alpha(n) > 1$, they can be expressed as

$$f_{MP}(n) = \begin{cases} \left|\frac{f_{shift}(n)}{1-\alpha(n)}\right|, \text{maximun} \\ \left|\frac{f_{shift}(n)}{1+\alpha(n)}\right|, \text{minimum} \end{cases} \tag{B.3}$$

Vice versa for cases when $\alpha(n) < 1$.

REFERENCES

[1] E. D. Kaplan and C. Hegarty, *Understanding GPS/GNSS: Principles and Applications*, 3rd ed. Boston, MA, USA: Artech House, 2017.

[2] E. S. Lohan and K. Borre, "Accuracy limits in multi-GNSS," *IEEE Trans. Aerosp. Electron. Syst.*, vol. 52, no. 5, pp. 2477–2494, 2016.

[3] Y. Qi, Z. Yao, and M. Lu, "General design methodology of code multi-correlator discriminator for GNSS multi-path mitigation," *IET Radar, Sonar & Navigation*, vol. 15, no. 9, pp. 969–984, 2021.

[4] A. Van Dierendonck, P. Fenton, and T. Ford, "Theory and performance of narrow correlator spacing in a GPS receiver," *Navigation*, vol. 39, no. 3, pp. 265–283, 1992.

[5] B. Townsend and P. Fenton, "A practical approach to the reduction of pseudorange multipath errors in a L1 GPS receiver," in *Proceedings of the 7th International Technical Meeting of the Satellite Division of the Institute of Navigation, Salt Lake City, UT, USA*, 1994, pp. 143–148.

[6] G. A. McGraw and M. S. Braasch, "GNSS multipath mitigation using gated and high resolution correlator concepts," in *Proceedings of the 1999 national technical meeting of the institute of navigation*, 1999, pp. 333–342.

[7] Y. Sun, Z. Yao, and M. Lu, "Extended double-delta correlator technique for GNSS multipath mitigation," *IEEE Trans. Aerosp. Electron. Syst.*, vol. 59, no. 2, pp. 1758–1773, 2022.

[8] P. C. Fenton and J. Jones, "The theory and performance of NovAtel Inc.'s vision correlator," in *Proceedings of the 18th International Technical Meeting of the Satellite Division of The Institute of Navigation (ION GNSS 2005)*, 2005, pp. 2178–2186.

[9] H. Li, P. Borhani-Darian, P. Wu, and P. Closas, "Deep neural network correlators for GNSS multipath mitigation," *IEEE Trans. Aerosp. Electron. Syst.*, vol. 59, no. 2, pp. 1249–1259, 2022.

[10] T. Suzuki and Y. Amano, "NLOS multipath classification of GNSS signal correlation output using machine learning," *Sensors*, vol. 21, no. 7, p. 2503, 2021.

$$f_0(n) = f_{LOS}(n) + \left(f_{ref}(n) - f_{LOS}(n)\right)\left(\frac{\alpha(n)\cos\left(\int_{t_0}^{t_n} 2\pi\left(f_{ref}(\tau) - f_{LOS}(\tau)\right)d\tau + \Delta\phi_{ref}(t_0) - \Delta\phi_{LOS}(t_0)\right) + 1}{\alpha^2(n) + 2\alpha(n)\cos\left(\int_{t_0}^{t_n} 2\pi\left(f_{ref}(\tau) - f_{LOS}(\tau)\right)d\tau + \Delta\phi_{ref}(t_0) - \Delta\phi_{LOS}(t_0)\right) + 1}\right) + v_{mea}(n) \quad \text{(A.9)}$$

[11] R. D. Van Nee, J. Siereveld, P. C. Fenton, and B. R. Townsend, "The multipath estimating delay lock loop: approaching theoretical accuracy limits," in *Proceedings of 1994 IEEE Position, Location and Navigation Symposium-PLANS'94*. IEEE, 1994, pp. 246–251.

[12] X. Chen, F. Dovis, S. Peng, and Y. Morton, "Comparative studies of GPS multipath mitigation methods performance," *IEEE Trans. Aerosp. Electron. Syst.*, vol. 49, no. 3, pp. 1555–1568, 2013.

[13] N. Blanco-Delgado and F. D. Nunes, "Multipath estimation in multicorrelator GNSS receivers using the maximum likelihood principle," *IEEE Trans. Aerosp. Electron. Syst.*, vol. 48, no. 4, pp. 3222–3233, 2012.

[14] X. Qi, B. Xu, Z. Wang, and L.-T. Hsu, "Random forest-based multipath parameter estimation," *GPS Solutions*, vol. 28, no. 126, 2024.

[15] Y. Wang and Z. Huang, "MEDLL on-strobe correlator: a combined anti-multipath technique for GNSS signal tracking," *J. Navig.*, vol. 73, no. 3, pp. 658–677, 2020.

[16] A. Pirsiavash, A. Broumandan, and G. Lachapelle, "Characterization of signal quality monitoring techniques for multipath detection in GNSS applications," *Sensors*, vol. 17, no. 7, p. 1579, 2017.

[17] A. Pirsiavash, A. Broumandan, G. Lachapelle, and K. O'keefe, "GNSS code multipath mitigation by cascading measurement monitoring techniques," *Sensors*, vol. 18, no. 6, p. 1967, 2018.

[18] P. Xu, G. Zhang, Y. Zhong, B. Yang, and L.-T. Hsu, "A framework for graphical GNSS multipath and nlos mitigation," *IEEE Trans. Intell. Transp. Syst.*, vol. 25, no. 9, pp. 12 176–12 186, 2024.

[19] Z. Jiang and P. D. Groves, "GNSS NLOS and multipath error mitigation using advanced multi-constellation consistency checking with height aiding," in *Proceedings of the 25th International Technical Meeting of the Satellite Division of the institute of navigation (ION GNSS 2012)*, 2012, pp. 79–88.

[20] J. Lesouple, T. Robert, M. Sahmoudi, J.-Y. Tourneret, and W. Vigneau, "Multipath mitigation for GNSS positioning in an urban environment using sparse estimation," *IEEE Trans. Intell. Transp. Syst.*, vol. 20, no. 4, pp. 1316–1328, 2018.

[21] H. Yuan, Z. Zhang, X. He, Y. Wen, and J. Zeng, "An extended robust estimation method considering the multipath effects in GNSS real-time kinematic positioning," *IEEE Trans. Instrum. Meas.*, vol. 71, pp. 1–9, 2022.

[22] P. D. Groves and Z. Jiang, "Height aiding, C/N0 weighting and consistency checking for GNSS NLOS and multipath mitigation in urban areas," *J. Navig.*, vol. 66, no. 5, pp. 653–669, 2013.

[23] N. S. Gowdayyanadoddi, J. T. Curran, A. Broumandan, and G. Lachapelle, "A ray-tracing technique to characterize GPS multipath in the frequency domain." *Int. J. Navigation Observation*, vol. 2015, 2015, Art. no. 983124.

[24] P. Xie and M. G. Petovello, "Measuring GNSS multipath distributions in urban canyon environments," *IEEE Trans. Instrum. Meas.*, vol. 64, no. 2, pp. 366–377, 2014.

[25] X. Chen, D. He, and L. Pei, "BDS B1I multipath channel statistical model comparison between static and dynamic scenarios in dense urban canyon environment," *Satellite Navigation*, vol. 1, no. 26, 2020.

[26] M. Irsigler, "Characterization of multipath phase rates in different multipath environments," *GPS Solutions*, vol. 14, pp. 305–317, 2010.

[27] C. Siebert, A. Konovaltsev, and M. Meurer, "Development and validation of a multipath mitigation technique using multi-correlator structures," *Navig. J. Inst. Navig.*, vol. 70, no. 4, 2023.

[28] G. Brodin and P. Daly, "GNSS code and carrier tracking in the presence of multipath," *Int. J. Satell. Commun.*, vol. 15, no. 1, pp. 25–34, 1997.

[29] J. Fang, L. Zhang, G. Zhang, B. Xu, and L.-T. Hsu, "Characterization and validation of GNSS multipath-induced Doppler measurement error," *IEEE Trans. Aerosp. Electron. Syst.*, vol. 61, no. 2, pp. 3498–3515, 2024.

[30] H.-F. Ng, L.-T. Hsu, M. J. L. Lee, J. Feng, T. Naeimi, M. Beheshti, and J.-R. Rizzo, "Real-time loosely coupled 3DMA GNSS/Doppler measurements integration using a graph optimization and its performance assessments in urban canyons of New York," *Sensors*, vol. 22, no. 17, p. 6533, 2022.

[31] H.-F. Ng, L.-T. Hsu, and G. Zhang, "Multi-epoch kriging-based 3D mapping-aided GNSS and doppler measurement fusion using factor graph optimization," *Navig. J. Inst. Navig.*, vol. 70, no. 4, 2023.

[32] L. Li, J. Zhong, and M. Zhao, "Doppler-aided GNSS position estimation with weighted least squares," *IEEE Trans. Veh. Technol.*, vol. 60, no. 8, pp. 3615–3624, 2011.

[33] M. Bahrami and M. Ziebart, "A Kalman filter-based Doppler-smoothing of code pseudoranges in GNSS-challenged environments," in *Proceedings of the 24th International Technical Meeting of the Satellite Division of The Institute of Navigation (ION GNSS 2011)*, 2011, pp. 2362–2372.

[34] Z. Zhou and B. Li, "Optimal Doppler-aided smoothing strategy for GNSS navigation," *GPS Solutions*, vol. 21, pp. 197–210, 2017.

[35] M. Bahrami and M. Ziebart, "Instantaneous Doppler-aided RTK positioning with single frequency receivers," in *IEEE/ION Position, Location and Navigation Symposium*. IEEE, 2010, pp. 70–78.

[36] G. Zhang, B. Xu, H.-F. Ng, and L.-T. Hsu, "GNSS RUMS: GNSS realistic urban multiagent simulator for collaborative positioning research," *Remote Sens.*, vol. 13, no. 4, p. 544, 2021.

[37] P. Misra and P. Enge, *Global positioning system: signals, measurements, and performance*, 2nd ed. New York, NY, USA: Ganga-Jamuna Press, 2006.

[38] K. Borre, D. M. Akos, N. Bertelsen, P. Rinder, and S. H. Jensen, *A software-defined GPS and Galileo receiver: a single-frequency approach*. MA, Boston: Birkhuser, 2007.

[39] P. R. Strode and P. D. Groves, "GNSS multipath detection using three-frequency signal-to-noise measurements," *GPS Solutions*, vol. 20, pp. 399–412, 2016.

[40] B. W. Parkinson and J. J. Spilker, *Global positioning system: Theory and Applications Volume I*. Washington, DC, USA: AIAA, 1996, pp. 379–385.

[41] S. Li, R. Yang, and X. Zhan, "Characterization of multi-band GNSS multipath in urban canyons using the 3D ray-tracing method," *GPS Solutions*, vol. 28, no. 49, 2024.

[42] C. Sun, H. Zhao, W. Feng, and S. Du, "A frequency-domain multipath parameter estimation and mitigation method for BOC-modulated GNSS signals," *Sensors*, vol. 18, no. 3, p. 721, 2018.

[43] J. Tu, X. Zhan, M. Chen, H. Gao, and Y. Chen, "GNSS intermediate spoofing detection via dual-peak in frequency domain and relative velocity residuals," *IET Radar Sonar Navig.*, vol. 14, no. 3, pp. 439–447, 2020.

[44] N. Linty and L. L. Presti, "Doppler frequency estimation in GNSS receivers based on double FFT," *IEEE Trans. Veh. Technol.*, vol. 65, no. 2, pp. 509–524, 2015.

[45] J. Nocedal and S. J. Wright, *Numerical optimization*. Springer, 1999.

[46] S. M. Kay, “Fundamentals of statistical signal processing: Estimation theory,” 1993.
[47] S. Kennedy, J. Hamilton, and H. Martell, “Architecture and system performance of SPAN-NovAtel’s GPS/INS solution,” in *Proceedings of IEEE/ION PLANS 2006*, 2006, pp. 266–274.
[48] L.-T. Hsu, F. Huang, H.-F. Ng, G. Zhang, Y. Zhong, X. Bai, and W. Wen, “Hong Kong UrbanNav: An open-source multisensory dataset for benchmarking urban navigation algorithms,” *Navig. J. Inst. Navig.*, vol. 70, no. 4, 2023.
[49] H.-F. Ng, G. Zhang, and L.-T. Hsu, “A computation effective range-based 3D mapping aided GNSS with NLOS correction method,” *J. Navig.*, vol. 73, no. 6, pp. 1202–1222, 2020.
[50] N. Sokhandan, J. T. Curran, A. Broumandan, and G. Lachapelle, “An advanced GNSS code multipath detection and estimation algorithm,” *GPS Solutions*, vol. 20, pp. 627–640, 2016.
[51] Y. Wang, Y. Kou, Z. Huang, and Y. Zhao, “GNSS spoofing maximum-likelihood estimation switching between MEDLL and CADLL,” *GPS Solutions*, vol. 27, no. 148, 2023.
[52] X. Qi and B. Xu, “Modelling and assessing reinforcement learning-assisted GNSS multipath estimation and mitigation for urban navigation,” *IEEE Trans. Veh. Technol.*, pp. 1–16, 2025.
[53] Y. Wang, X. Chen, and P. Liu, “Statistical multipath model based on experimental GNSS data in static urban canyon environment,” *Sensors*, vol. 18, no. 4, p. 1149, 2018.
[54] L.-T. Hsu, “GNSS multipath detection using a machine learning approach,” in *2017 IEEE 20th international conference on intelligent transportation systems (ITSC)*. IEEE, 2017, pp. 1–6.

Jingxiaotao Fang received her bachelor’s degree in the Department of Aeronautical and Aviation Engineering from The Hong Kong Polytechnic University in 2022. She is currently a Ph.D. candidate at the Department of Aeronautical and Aviation Engineering, The Hong Kong Polytechnic University, Hong Kong. Her research interests include GNSS signal processing for GNSS navigation accuracy and security.

Bing Xu (Member, IEEE) is currently an Assistant Professor with the Department of Aeronautical and Aviation Engineering, The Hong Kong Polytechnic University, Hong Kong. Prior to the current post, he was Postdoctoral Fellow and Research Assistant Professor with the same institute. He received his BEng and Ph.D. degrees from Nanjing University of Science and Technology in 2012 and 2018, respectively. His research focuses on GNSS signal processing and its applications to multipath and spoofing problems. He is also interested in LEO navigation and cellular signal positioning.

Xikun Liu received his bachelor’s degree in Mechanical Design, Manufacturing, and Automation from Huazhong University of Science and Technology, China in 2017, and master’s degree in Mechatronics and Information Technology from Karlsruhe Institute of Technology, Germany in 2021. He is currently a Ph.D. candidate in the Department of Aeronautical and Aviation Engineering, the Hong Kong Polytechnic University. His research interests include GNSS and sensor-aided GNSS positioning, SLAM, and multiple sensor fusion in autonomous driving.

Li-Ta Hsu (Senior Member, IEEE) received the B.S. and Ph.D. degrees in aeronautics and astronautics from National Cheng Kung University, Tainan, Taiwan, in 2007 and 2013, respectively. He was a Visiting Researcher with the Faculty of Engineering, University College London and Tokyo University of Marine Science and Technology, in 2012 and 2013, respectively. He was a JSPS Postdoctoral Fellow with The University of Tokyo, from 2014 to 2016. He is currently an Associate Professor with the Department of Aeronautical and Aviation Engineering, Hong Kong Polytechnic University, Hong Kong.

Dr. Hsu is Limin Endowed Young Scholar in Aerospace Navigation. He is an Associate Fellow with the Royal Institute of Navigation. He is currently a Member of the Institute of Navigation and serves as a Member of the editorial board and a Reviewer in professional journals related to navigation and global navigation satellite system.